USGS
science for a changing world

Postwildfire Measurement of Soil Physical and Hydraulic Properties at Selected Sampling Sites in the 2011 Las Conchas Wildfire Burn Scar, Jemez Mountains, North-Central New Mexico

Scientific Investigations Report 2018–5028

U.S. Department of the Interior
U.S. Geological Survey

Cover: A soil-core sample, prior to removal from the ground, from Las Conchas burn scar, Jemez Mountains, North-Central New Mexico, June, 2015.

Postwildfire Measurement of Soil Physical and Hydraulic Properties at Selected Sampling Sites in the 2011 Las Conchas Wildfire Burn Scar, Jemez Mountains, North-Central New Mexico

By Orlando C. Romero, Brian A. Ebel, Deborah A. Martin, Katie W. Buchan, and Alanna D. Jornigan

Scientific Investigations Report 2018–5028

U.S. Department of the Interior
U.S. Geological Survey

U.S. Department of the Interior
RYAN K. ZINKE, Secretary

U.S. Geological Survey
William H. Werkheiser, Acting Director
exercising the authority of the Director

U.S. Geological Survey, Reston, Virginia: 2018

Suggested citation:
Romero, O.C., Ebel, B.A., Martin, D.A., Buchan, K.W., and Jornigan, A.D., 2018, Postwildfire measurement of soil physical and hydraulic properties at selected sampling sites in the 2011 Las Conchas wildfire burn scar, Jemez Mountains, north-central New Mexico: U.S. Geological Survey Scientific Investigations Report 2018–5028, 35 p., https://doi.org/10.3133/sir20185028.

ISSN 2328-0328 (online)

Acknowledgments

This project was funded by U.S. Geological Survey Southwest Region Wildfire Science Project funds. This project would not have been possible without assistance from the Santa Fe National Forest staff to facilitate field site access. The authors would like to thank Aurelia Mitchell for her GIS assistance, Keely Miltenberger for checking laboratory measurements and other administrative tasks, and John A. Moody and Jeb E. Brown for their thorough and helpful peer reviews of this report.

Contents

Figures

Tables

Conversion Factors

International System of Units to U.S. customary units

Multiply	By	To obtain
	Length	
centimeter (cm)	0.3937	inch (in.)
millimeter (mm)	0.03937	inch (in.)
meter (m)	3.281	foot (ft)
kilometer (km)	0.6214	mile (mi)
	Area	
hectare (ha)	2.471	acre
square kilometer (km^2)	247.1	acre
square kilometer (km^2)	0.3861	square mile (mi^2)
	Volume	
cubic meter (m^3)	0.0002642	million gallons (Mgal)
cubic meter (m^3)	35.31	cubic foot (ft^3)
cubic meter (m^3)	1.308	cubic yard (yd^3)
cubic meter (m^3)	0.0008107	acre-foot (acre-ft)

Temperature in degrees Celsius (°C) may be converted to degrees Fahrenheit (°F) as

$$°F = (1.8 \times °C) + 32.$$

Datum

Vertical coordinate information is referenced to the North American Vertical Datum of 1988 (NAVD 88).

Horizontal coordinate information is referenced to the North American Datum of 1983 (NAD 83).

Abbreviations

BARC	Burned Area Reflectance Classification
CI	Cumulative infiltration
CL	Cumulative Linearization
DL	Differentiated Linearization
dNBR	difference in the Normalized Burn Ratio
K_{fs}	field saturated hydraulic conductivity
K_s	saturated hydraulic conductivity
MTBS	Monitoring Trends in Burn Severity
NBR	Normalized Burn Ratio
NMWSC	New Mexico Water Science Center
S	sorptivity
SHP	soil-hydraulic properties
SPP	soil-physical properties
USGS	U.S. Geological Survey

Postwildfire Measurement of Soil Physical and Hydraulic Properties at Selected Sampling Sites in the 2011 Las Conchas Wildfire Burn Scar, Jemez Mountains, North-Central New Mexico

By Orlando C. Romero, Brian A. Ebel, Deborah A. Martin, Katie W. Buchan, and Alanna D. Jornigan

Abstract

The generation of runoff and the resultant flash flooding can be substantially larger following wildfire than for similar rainstorms that precede wildfire disturbance. Flash flooding after the 2011 Las Conchas Fire in New Mexico provided the motivation for this investigation to assess postwildfire effects on soil-hydraulic properties (SHPs) and soil-physical properties (SPPs) as a function of remotely sensed burn severity 4 years following the wildfire. A secondary purpose of this report is to illustrate a methodology to determine SHPs that analyzes infiltrometer data by using three different analysis methods. The SPPs and SHPs are measured as a function of remotely sensed burn severity by using the difference in the Normalized Burn Ratio (dNBR) metric for seven sites. The dNBR metric was used to guide field sample collection across a full spectrum of burn severities that covered the range of Monitoring Trends in Burn Severity (MTBS) and Burned Area Reflectance Classification (BARC) thematic classes from low to high severity. The SPPs (initial and saturated soil-water content, bulk density, soil-organic matter, and soil-particle size) and SHPs (field-saturated hydraulic conductivity and sorptivity) were measured under controlled laboratory conditions for soil cores collected in the field. The SHPs were estimated by using tension infiltrometer measurements and three different data analysis methods. These measurements showed large effects of burn severity, focused in the top 1 centimeter (cm) of soil, on some SPPs (bulk density, soil organic matter, and particle sizes). The threshold of these bulk density and soil organic matter effects was between 300 and 400 dNBR, which corresponds to a MTBS thematic class between moderate and high burn severity and a BARC4 thematic class of high severity. Gravel content and the content of fines in the top 1 cm of soil had a higher threshold value between 450 and 500 dNBR. Lesser effects on SPPs were observed at depths of 1–3 cm and 3–6 cm. In contrast, SHPs showed little effect from dNBR or from MTBS/BARC4 thematic class. Measurements suggested that 4 years of elapsed time after the wildfire may be sufficient for SHP recovery in this area. These measurements also indicated that SPP differences as a function of burn severity cannot be used as reliable indicators of SHP differences as a function of burn severity.

Introduction

In the past three decades, the frequency, severity, and extent (burned area) of wildfires have steadily increased in the United States (U.S. Environmental Protection Agency, 2016). This increase is especially true in the western United States where the frequency of large wildfires and their extent has increased by six times since the mid-1980s (National Wildlife Federation, 2008). There are many reasons for the increases in frequency, severity, and extent, including drought, increases in average seasonal temperatures, increased fuel loads, and longer fire seasons (Patterson, 1997; National Wildlife Federation, 2008). In addition, some of the reasons originate from human activity and are either indirectly tied to increases in human population in the wildland-urban interface or directly tied to increases in actual human ignitions (Balch and others, 2017).

Although often used interchangeably, the phrases “burn intensity” and “burn severity” are not equivalent. “Burn intensity” refers to the magnitude of heat and energy released during a fire and is therefore a function of temperature and fire duration. “Burn severity,” however, refers to the effects of a fire and although closely related to intensity, the term can encompass not only environmental and ecological effects but socioeconomic effects as well (Key and Benson, 2006).

The extreme heat and energy release that are generated in high-intensity wildfires create an increase in hydrophobicity, or water repellency, above the natural water repellency that exists in all soils (Doerr and others, 2000; Letey, 2001; National Wildfire Coordinating Group, 2006; Tillery and others, 2011; Moody and others, 2016). Additionally,

areas that have been subjected to high-intensity fire are characterized by a near-total consumption of the prewildfire organic cover, including canopy vegetation, litter, duff, and fine roots (Keely, 2009; Parsons and others, 2010; Tillery and others, 2011). These combined characteristics of high-severity burn scars can cause increased susceptibility to flooding and large debris flows, which are overland flows of mixtures of water, rock, soil, ash, and organic materials (Tillery and others, 2011). The flooding and debris flows, together or separately, possess considerable potential for destruction and present a substantial threat to life and property in the watershed. The loss of soil productivity can also delay vegetation regeneration and recolonization in the severely burned areas, resulting in a nonvegetated area that sheds water rapidly and continues the cycle of flooding and debris flows (Tillery and others, 2011).

Quantifying the threat of flooding or debris flows from wildfire burn scars can be challenging. The remoteness and sheer size of many burn scars create difficulties in collecting samples and other field data that are a necessity to quantifying the hydrologic and other environmental effects of wildfires. The situation is further complicated because potential postwildfire effects can last for years, and the effects are especially pronounced in the first 2–3 years following a wildfire (Tillery and others, 2011; U.S. Department of Agriculture [USDA]–Forest Service [FS], 2011). In response to these difficulties, scientists have recognized the need for a method to rapidly assess potential postwildfire hazards over large areas with as little direct sampling as possible (Cocke and others, 2005; Garrity and others, 2013). However, a fundamental problem in predicting postwildfire runoff and erosion is the incomplete understanding of the links between burn severity and the soil physical properties (SPPs) and soil hydraulic properties (SHPs) that control infiltration, and thus, runoff generation (Moody and others, 2016). To address this disconnect, Moody and others (2016) have used controlled laboratory measurements of soil properties of intact field soil samples at discrete sites to determine relations with a remotely sensed, more spatially continuous burn-severity metric available over the entire burned area. More specifically, the burn-severity metric that was used for the comparison was the difference in Normalized Burn Ratio (dNBR), which is a metric based on changes in surface reflectance measured in Landsat satellite images collected before and after a wildfire (Key and Benson, 2006).

The field site selected in this study to examine relations between the remotely sensed burn-severity metric dNBR and soil properties was the burn scar of the 2011 Las Conchas Fire. This wildfire burned 63,372 hectares (ha) of mixed conifer, pinyon juniper, and ponderosa forest in the Jemez Mountains of north-central New Mexico (fig. 1) and made history at the time as the largest recorded wildfire in New Mexico (Tillery and others, 2011; USDA–FS, 2011; Trader, 2012). The extreme behavior of the fire was the result of converging biotic and abiotic variables; high soil moisture during the 2009–10 growing season caused maximal vegetative growth in the Jemez Mountains, and subsequent La Niña conditions during the 2010–11 winter seasons caused below normal precipitation and intensified existing drought conditions (Trader, 2012; Schoeffler and Wachter, 2015). Postwildfire analysis shows varying burn severity across the burn scar, with about 23 percent of the area characterized as high severity and 25 percent characterized as moderate severity (USDA–FS, 2011) (fig. 2). The fire created an estimated 14,000 ha of hydrophobic soils across the burned landscape (USDA–FS, 2011). In addition, sediment erosion potential over the burned area was estimated at more than 1,900 cubic meters/square kilometer (m^3/km^2) (USDA–FS, 2011).

Much of the severely burned area was on steep upland sites at the headwaters of multiple watersheds, increasing the potential of flooding and debris flows immediately following the fire (Tillery and others, 2011; USDA–FS, 2011). At the inception of this study in 2015, large overland flows were still observed in watersheds severely burned by the Las Conchas Fire. Despite some vegetative recovery, soil erosion and overland flows will most likely continue to be a threat to communities for years to come (Tillery and others, 2011). For this reason, the Las Conchas Fire presented an excellent opportunity to examine the relation between remotely sensed dNBR values and soil properties multiple years after a severe wildfire.

Purpose and Scope

The primary purpose of this report is to assess postwildfire measurements of SPPs and SHPs as a function of remotely sensed burn severity 4 years following wildfire in the Southern Rocky Mountains of New Mexico. The SHPs examined were field-saturated hydraulic conductivity (K_{fs}) and sorptivity (S), and the SPPs examined were bulk density, saturated soil-water content, soil-organic matter, and particle-size distribution. A secondary purpose of this report is to illustrate a methodology to determine SHPs that use cumulative infiltrometer data combined with the collective application of three different analysis methods.

Description of Las Conchas Fire and Study Area

The Las Conchas Fire burned an area in the Jemez Mountains of north-central New Mexico (fig. 1) during 2011. It was ignited on June 26, 2011, when a falling tree made contact with a powerline; by the time the fire was contained on August 3, 2011, it had burned over 63,000 ha of forest and damaged or destroyed more than 100 structures (USDA–FS, 2011). Postwildfire flooding in the following months and years caused significant damage to communities downstream from the burned watersheds. Areas affected by the fire included the Santa Fe National Forest; the Valles Caldera National Preserve; Bandelier National Monument; the Jemez, Santa Clara, Cochiti, and Santo Domingo Pueblos; and private lands (USDA–FS, 2011; Schoeffler and Wachter, 2015).

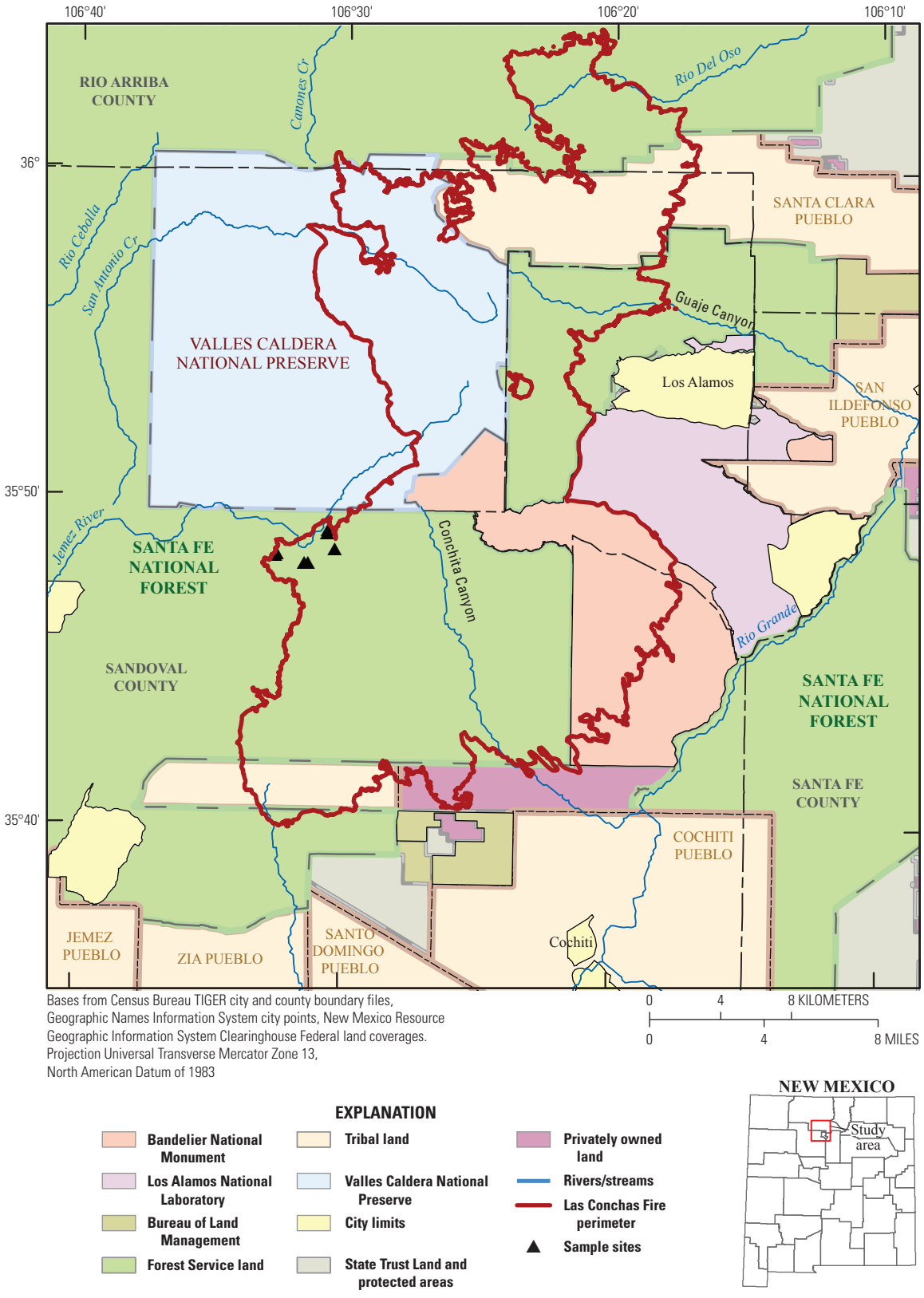

Figure 1. The Las Conchas Fire perimeter in the Jemez Mountains, surrounding land management agencies, and sampling sites in north-central New Mexico. Inset rectangle shows area of figure 2.

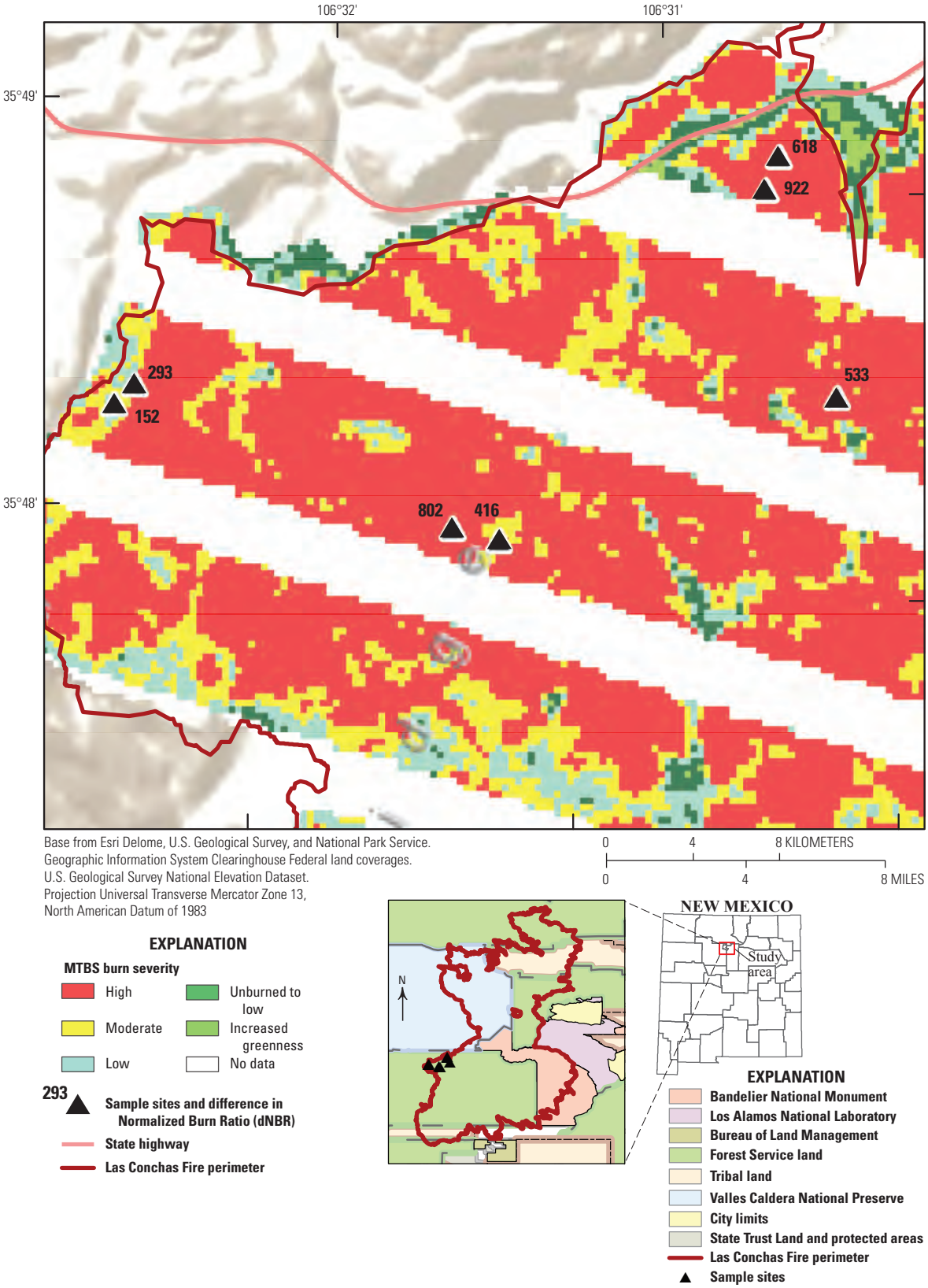

Figure 2. Burn-severity map from Monitoring Trends in Burn Severity (2017) used for site selection in Las Conchas study area. Minor map shows sample sites relative to entire Las Conchas Fire perimeter. Unmapped, banded stripes in the imagery are the result of Landsat 7 errors at the time of the postwildfire image. Image has a resolution, or pixel size, of 30 meters.

Although the Las Conchas Wildfire varied in burn severity (fig. 2) and encompassed several landscape types and topographies, it burned in mostly mountainous terrain with predominantly steep slopes and elevations ranging from about 1,800 meters (m) to 2,700 m. Soils are primarily Mollic Eutroboralfs/Andic Ustochrepts/Typic Ustorthents, viltrandic hapludalfs, viltrandic eutrocryepts, and pachic argiustolls (USDA–FS, 2011). Volcanic tuff- and pumice-derived soils are productive but have very high erosion potentials because of low bulk density of extrusive volcanic parent material (USDA–FS, 2011). Bulk density is a measurement of general soil density and can affect water and solute movement; erosion potential; soil aeration; and other physical, chemical, and biological properties of the soil (USDA, Natural Resources Conservation Service [NRCS], 2008). There are approximately 160 kilometers (km) of perennial streams and 440 km of ephemeral and intermittent streams within the burn perimeter (USDA–FS, 2011).

Sampling sites, identified by "LC" and dNBR burn severity, were located in vegetation communities that prior to the 2011 wildfire were dominated by stands of various mixed conifers. Sites LC–152, LC–293, LC–618 and LC–922 (fig. 2) were in stands composed primarily of *Pseudotsuga menziesii* (Mirb.) Franco var. *glauca* (Beissn.) Franco (Douglas fir), and sites LC–416 and LC–533 were in stands primarily of *Abies concolor* (Gord. & Glend.) Lindl. ex Hildebr. (white fir). Site LC–802, however, was in a stand dominated mostly by *Populus tremuloides* Michx. (aspen) before the 2011 burn (University of California Davis Soil Resource Laboratory, 2016). All sites were reclassified as "burned" in 2012 except for the low-burn severity sites LC–152 and LC–293, which remained primarily composed of unburned Douglas fir.

Methods and Approach

Seven soil sampling sites in the burned area were chosen on the basis of different values of the dNBR metric and resultant burn-severity classifications. The thematic burn-severity classifications used in this study are the Monitoring Trends in Burn Severity (MTBS) program (2017) mapping and the Burned Area Emergency Response (BAER) Burned Area Reflectance Classification (BARC4) mapping (U.S. Forest Service, 2017). These classifications are based on the dNBR metric but also incorporate field observations and measurements to determine overall burn severity. Sample sites were chosen on the basis of the dNBR metric itself but with the goal that the sites also cover the full spectrum of burn severities, from low to high, within the range of MTBS and BARC4 thematic classes.

Fourteen replicate soil core samples, randomly selected at the sampling sites, were collected from each of the seven sampling sites. Of these 14 samples, 4 were used to measure SPPs, and 10 were used to measure SHPs. The SPPs were analyzed at the U.S. Geological Survey (USGS) National Research Program offices in Boulder, Colorado, and SHPs of intact soil cores were measured in the USGS Water Quality Laboratory at the USGS New Mexico Water Science Center (NMWSC) by using a tension infiltrometer. The infiltrometer measurements were analyzed by using three separate methods to assess uncertainty (methods adapted from Vandervaere and others, 2000; Moody and others, 2016).

Statistical analyses of data were performed with Microsoft Excel software by using the Fischer F-test (Fischer, 1922). All data used in the analyses in this report are available from a USGS data release (Ebel and Romero, 2017).

Determination of Burn Severity

The USGS Earth Resources Observation and Science Center (EROS) provided a burn-severity map of the Las Conchas Fire with dNBR values based on a prewildfire image obtained on June 24, 2011, from Landsat 5 and a postwildfire image obtained on June 18, 2012, from Landsat 7 (fig. 2). The Landsat program utilizes satellites to collect multispectral images from around the globe (National Aeronautics and Space Administration, 2017). Both Landsat images used to determine soil sampling sites have an image resolution, or pixel size, of 30 m (National Aeronautics and Space Administration, 2017). At the time of the postwildfire image, the Landsat 7 satellite was failing, resulting in unmapped, banded stripes in the imagery; however, the locations of all study sites were selected to be in the available prewildfire and postwildfire imagery. The basic index of remotely sensed burn severity is determined by using the Normalized Burn Ratio (NBR) method, which uses satellite imagery for bands that respond well to burn characteristics (bands 4 and 7) to establish reflectance (*R*) values. These values are then used to generate NBR values with the equation (Key and Benson, 2006):

$$NBR = (R4 - R7)/(R4 + R7), \quad (1)$$

Values of NBR are converted to integer values by multiplying by 1,000. The difference between prewildfire ($NBR_{prewildfire}$) and postwildfire *NBR* ($NBR_{postwildfire}$) is the dNBR value:

$$dNBR = NBR_{prewildfire} - NBR_{postwildfire}, \quad (2)$$

which provides a quantitative measure of the difference in NBR values between isolated burned and unburned areas (Keeley, 2009; Moody and others, 2016). The common range for dNBR varies from -100 (unburned) to +1,000 (high severity burn) although measured dNBR values can fall outside of this range. Reflectance in band 4 responds to live vegetation chlorophyll content and reflectance in band 7 responds to soil and vegetation water content, nonphotosynthetic vegetation, and hydrous minerals in soils

(Miller and Thode, 2007). The dNBR burn-severity metric captures changes following wildfire in living photosynthetic vegetation, vegetation and soil moisture content, and changes in the soil surface (Miller and Thode, 2007). These dNBR values are used to create a MTBS thematic burn-severity class map that delineates ecological burn severity into the following classes: increased greenness, unburned, low, moderate, and high. For the Las Conchas Fire, the thresholds for the MTBS thematic burn-severity classes relative to dNBR values were (1) increased greenness/unchanged/unburned corresponds to dNBR greater than -150 and less than 5; (2) low corresponds to dNBR greater than or equal to 5 and less than 177; (3) moderate corresponds to dNBR greater than or equal to 177 and less than 380; and (4) high corresponds to dNBR greater than or equal to 380.

Alternatively, the BAER mapping of burn-severity uses the BARC256 map, derived from dNBR and adjusted based on actual field observations, to develop a four-class thematic burn-severity map called the BARC4 map (U.S. Forest Service, 2017). For the Las Conchas Fire, the thresholds for the BARC4 thematic burn-severity classes relative to BARC256 values (ranging from 0 to 255) were (1) increased greenness/unchanged/unburned corresponds to less than 78; (2) low corresponds to greater than or equal to 78 and less than 112; (3) moderate corresponds to greater than or equal to 112 and less than 188; and (4) high corresponds to greater than or equal to 188.

In this study, both MTBS and BARC4 thematic burn-severity classifications were used to investigate relations between burn severity and soil properties. Burn severity and other details of sample collection sites are given in table 1.

Sampling Design and Sample Collection

The remotely sensed burn-severity metric dNBR guided sample collection across a full spectrum of burn severities that cover the range of MTBS and BARC4 thematic classes from low to high severity. Soil cores were collected from seven sites with varying dNBR values within the perimeter of the area burned by the Las Conchas Fire in 2011 (fig. 2). The seven selected sites correspond to different dNBR values: 152, 293, 416, 533, 618, 802, and 922 (table 1). Sample sites were selected such that the site (1) was surrounded by as many pixels as possible with the same burn-severity classification as the selected sample site (as much as eight pixels); (2) has the same soil type as the other six selected sample sites (USDA NRCS, 2016); and (3) is located in an area with reasonable vehicle or walking access. Fourteen random samples were then taken from within the 30-m perimeter surrounding each of the seven selected sampling sites, and these random samples were used for determining SPP and SHP. Details of sample collection sites are given in table 1.

The sampling area at each site was a 30-m diameter circle, based on the Landsat pixel size, the center of which was determined by using a Wide Area Augmentation System enabled, recreational-grade, hand-held Global Positioning System (GPS) unit. The 14 sample core locations within each sampling area were predetermined by using a map and a computer program to randomize distances and azimuths relative to the sampling area center (fig. 3). These distances and angles were then mapped in the field with tape measures and a large wooden circular protractor resting on an inverted bucket and oriented by using the GPS unit (fig. 4). Sampling

Table 1. Location of sample collection sites within the perimeter of the 2011 Las Conchas Fire and their respective burn severities.

[The geographic coordinate system is the North American 1983 (NAD 1983) datum. The remotely sensed burn-severity metric is the difference in the normalized burn ratio (dNBR) described by Key and Benson (2006). dNBR burn severity is based on the thematic burn-severity class from the Monitoring Trends in the Burn Severity program (MTBS). For the 2011 Las Conchas Fire, the MTBS classification based on dNBR values was unburned (dNBR<5), low (5≤dNBR<177), moderate (177≤dNBR<380), and high (dNBR≥380). Burned Area Reflectance Classification (BARC) burn-severity map (BARC4) is the dNBR-based BARC256 map adjusted by the Burned Area Emergency Response team for field conditions into 4 classes. BARC 256 thresholds for the BARC4 map were unburned (BARC256<78), low (78≤BARC256<112), moderate (112≤BARC256<188), and high (BARC256≥188). n is the number of samples; <, less than; >, greater than; ≥, greater than or equal; ≤, less than or equal; m, meters; (-), dimensionless; UTM E, Universal Transverse Mercator Easting; UTM N, Universal Transverse Mercator Northing]

Site name	dNBR	MTBS burn severity	BARC256	BARC4 burn severity	Date collected	UTM E	UTM N	Soil-hydraulic property cores	Soil-physical property core
	(-)	(-)	(-)	(-)	(2015)	(m)	(m)	n	n
LC–152	152	Low	91	Low	8 June	360620	3963352	10	4
LC–293	293	Moderate	106	Low	8 June	360706	3963449	10	4
LC–416	416	High	225	High	9 June	362462	3962897	10	4
LC–533	533	High	232	High	8 June	363965	3963694	10	4
LC–618	618	High	242	High	9 June	363588	3964763	10	4
LC–802	802	High	255	High	9 June	362243	3962932	10	4
LC–922	922	High	255	High	9 June	363541	3964608	10	4

Sampling party: Brian Ebel, Orlando Romero, John Moody, Deborah Martin

08 June 2015
Las Conchas Fire

SITE: 293 **2011 Las Conchas Fire**

Random Sampling in Circle with diameter = 15 m

Δ NBR value: 293

UTM Coordinates: 360706 E 3963449 N

	a=2pi* Rand	r= SQRT(Rand)					Soil Core ID	
	a (rad)	**r (m)**	**X (m)**	**Y (m)**	**Theta**	**R (m)**		
Cores: Soil Hydraulic Properties								
1	3.65	0.93	-12.20	-6.83	209	13.98	LC293-1	J
2	3.00	0.88	-13.00	1.81	172	13.13	LC293-2	B
3	3.38	0.68	-9.97	-2.41	194	10.26	LC293-3	J
4	1.16	0.16	0.99	2.26	66	2.47	LC293-4	B
5	1.84	0.10	-0.39	1.42	105	1.47	LC293-5	B
6	0.25	0.90	13.13	3.35	14	13.55	LC293-6	B
7	2.41	0.91	-10.18	9.07	138	13.64	LC293-7	J (Slitter/duff 77cm track left intact)
8	1.85	0.09	-0.37	1.32	106	1.38	LC293-8	B
9	2.48	0.71	-8.47	6.55	142	10.71	LC293-9	J
10	3.37	0.65	-9.52	-2.16	193	9.76	LC293-10	B
11	5.61	0.26	3.09	-2.45	322	3.95	LC293-11	J
12	3.97	0.57	-5.79	-6.34	228	8.59	LC293-12	B
Cores: Particle size, LOI, and WR								
13	X				93	14.43	LC293-13	J
14	X				46	14.05	LC293-14	B
	3							

Observations

Heavy use of this site by cattle, cow pies are fresh. Surface has more grass than site LC152 plus dandelions, mullein, and flea bane. JAM thinks this site is not grassier than LC152. The photos should give us some insights.

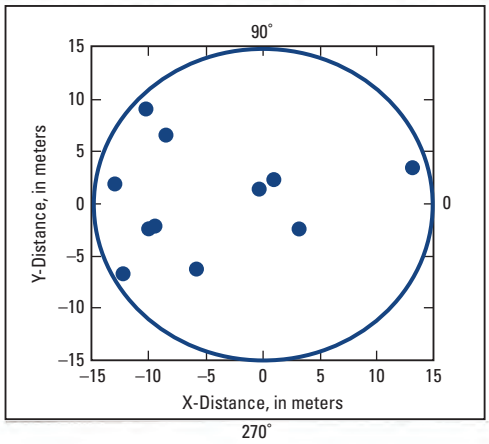

Left behind:

Washer labeled "293" on 1/2" rebar projecting 9.8 cm above ground (sampling center) and rebar projecting 2 cm above ground: 32.5 cm from center pin with blank washer.

Both washers were left at ground level.

Figure 3. Actual field notes for site LC–293. The pattern of random sampling is shown in the plot on the bottom. Note in the field notes that the diameter of the sampling circle is incorrectly listed as 15 meters (m); the true diameter of the sampling circle was 30 m.

Figure 4. *A*, U.S. Geological Survey (USGS) scientist holding the large wooden circular protractor prior to collection of soil core samples in the Las Conchas Fire burn scar; and *B*, USGS scientists using the protractor and measuring tapes to map the random sampling for site LC–293.

sites were visually inspected for general physical conditions such as canopy, understory vegetation, ground cover, litter, and signs of erosion. Soil cores (4.7 centimeters (cm) in diameter and 6 cm in length) were collected from sites LC–152, LC– 293, and LC–533 on June 8, 2015, and cores from sites LC–416, LC–618, LC–802, and LC–922 were collected on June 9, 2015. All collected samples encompassed the top 6 cm of the ground surface, which was the core length. All sample sites were photographed for reference and to aid in interpretation of the data (fig. 5). Each stainless-steel core tube was coated with petroleum jelly to prevent water from seeping down along the inside of the tube during infiltration measurements. Samples were collected by using a small hammer and wood block to pound the empty core into the ground. Cores were then capped on both ends upon extraction, labeled, and sealed with electrical tape. All sample cores from each site were brought back to the NMWSC and stored in an upright position, to maintain vertical soil structure, in a refrigerator for approximately 5 months. Four additional cores were taken at each site to determine the SPP of bulk density, saturated soil-water content, particle-size distribution, and organic matter content; these analyses were conducted at a USGS laboratory in Boulder, Colorado.

Laboratory Methods for Soil Physical Properties

The SPPs can be used to discern differences in physical properties between sites that may influence differences in SHPs between sites. The physical properties of interest are dry bulk density, organic matter content, soil-particle size, and initial (that is, “as sampled”) and saturated soil-water content. These properties were measured in the USGS soil laboratory in Boulder, Colorado, for four soil cores from each dNBR site. Dry bulk density was measured using the dry sample weight (24 hours at 105 degrees Celsius [°C]; Topp and Ferre, 2002) and the known core volume. Organic matter content was measured by using the Loss on Ignition technique, which volatilizes organic matter within the sample by heating a subsample at 500 °C for 2 hours

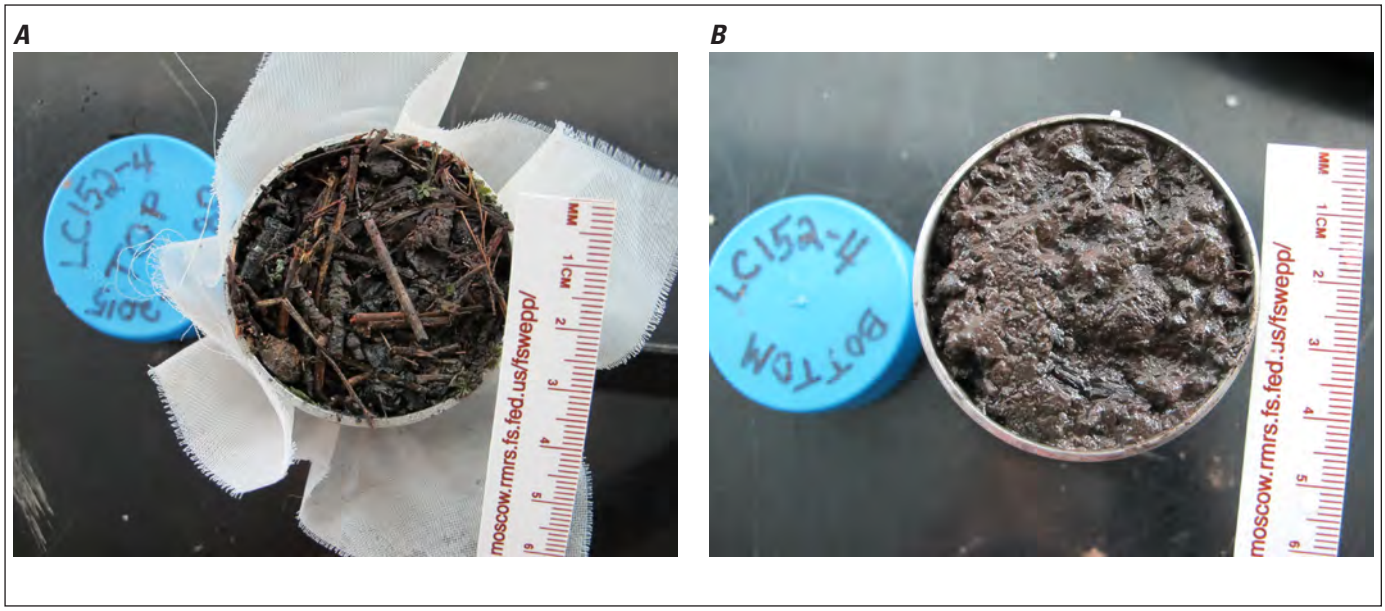

Figure 5. Soil core samples collected in the Las Conchas Fire burn scar. Top and bottom surfaces of the soil and core caps are the fourth sample from site LC–152.

(Heiri and others, 2001). Soil-particle size was estimated by using standard sieving methods (Guy, 1969). As a quality-control measure, for each sample the sum of the masses of individual particle-size classes after sieving was compared to the mass of the whole sample prior to sieving; mass differences that were greater than 5 percent are noted in the "Soil Physical Properties" section. Initial soil-water content was measured with the thermogravimetric method (24 hours at 105 °C; Topp and Ferre, 2002). Saturated soil-water content was estimated by the immersion of the cores in water for approximately 3 weeks, followed by drying with the thermogravimetric method (Topp and Ferre, 2002). Saturated soil-water content is a measure of the porosity of the soil and comparison to initial soil-water content can give insight into the determination of SHP.

Laboratory Methods for Soil Hydraulic Properties

The SHP were measured in the NMWSC water-quality laboratory by using a tension infiltrometer (Decagon Devices Mini Disk Infiltrometer). Tension infiltrometers apply water to the surface at a slight tension, or suction, to help minimize the effect of large macropores and structural differences in the soil and capture flow rates through the soil matrix (Ebel and others, 2012). Based on the results of prior laboratory experience with the mini-disk infiltrometer (Ebel and others, 2012), approximately 1 cm of suction (expressed here as equivalent hydraulic head) was applied for measurements made during this study.

The base of the soil core inside the core tube was covered with fine plastic mesh to prevent soil loss during measurement, and a 3–6 millimeter (mm) layer of contact sand was added to the top of the soil core to provide a uniform contact surface for the infiltrometer base. The soil core, inside the core tube, was placed on a plastic stand (fig. 6) with a hole in the center to allow water to move freely through the soil core and to prevent accumulation of water at the base. Tap water at an approximate temperature of 24 °C was placed in the reservoir chamber of the infiltrometer, and the sintered steel disc of the infiltrometer was placed flush with the surface of the contact sand inside a fitted orange plastic collar (fig. 6*B*) to prevent lateral loss of water and to stabilize the infiltrometer in a vertical position. Water was then added to the infiltrometer where it infiltrated into the soil core. The volume of water that infiltrated into the core and the corresponding length of time of infiltration was recorded incrementally from initial contact between the infiltrometer and sand to several seconds past the time that water had made its way fully through the soil core and was captured by a petri dish below.

Data Processing and Analysis for Soil Hydraulic Properties

To determine the SHPs of saturated hydraulic conductivity (K_s) and sorptivity (S), three different methods were used to analyze infiltration rate. These methods were cumulative infiltration, differentiated linearization, and cumulative linearization.

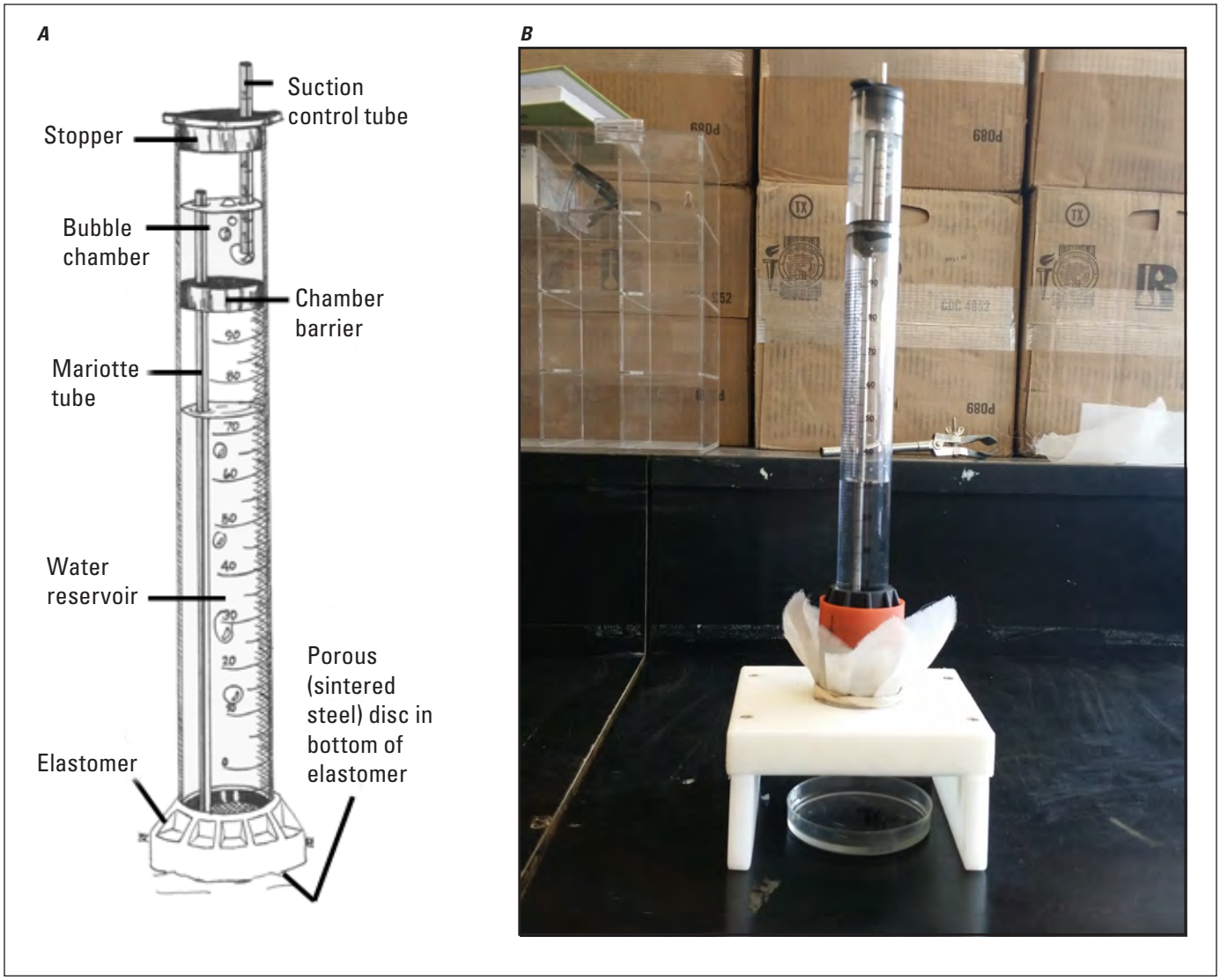

Figure 6. Infiltration setup: *A*, diagram of the mini-disk tension infiltrometer; and *B*, photograph showing an example setup of the infiltrometer prior to adding water for measurement of cumulative infiltration. A petri dish to collect water that passes through the core is underneath the plastic stand; the white material below the orange plastic collar is the mesh. Diagram of mini-disk tension infiltrometer used with permission from METER Group (Decagon Devices, 2013).

Cumulative Infiltration (CI)

Infiltration rate is a measurement of the depth of water (volume of water/surface area) absorbed through a given medium in a given amount of time. Cumulative infiltration is related to the soil properties K_s and S (Phillip, 1969):

$$I = St^{1/2} + Ct \quad (3)$$

where, I is cumulative infiltration (length);
S is sorptivity (length multiplied by inverse square root of time);
t is time; and
C is a coefficient (length divided by time) related to saturated hydraulic conductivity.

Substituting $x = t^{1/2}$ into equation 3 gives a quadratic equation of the form:

$$I = Sx + Cx^2 \quad (4)$$

As demonstrated by Zhang (1997), S and C can then be determined by fitting equation 4 to cumulative infiltration data as a function of the square root of time, yielding the corresponding coefficients of the x and x^2 terms. From Vandervaere and others (2000), the coefficient C is related to saturated hydraulic conductivity with the following term:

$$K_s = \frac{3C}{(2-\beta)} \quad (5)$$

where, K_s is saturated hydraulic conductivity (length/time);
C is a coefficient (length divided by time); and
β is a dimensionless coefficient.

The dimensionless coefficient β is dependent on hydraulic diffusivity and is assumed to be a constant value of 0.6 (Haverkamp and others, 1994). With known values of C and β, equation 5 can be used to determine K_s. With this method, cumulative infiltration data can be used with equations 4 and 5 to provide estimates of S and K_s, respectively.

The above equations that govern CI have been developed for ideal soil conditions. However, hydraulic conductivity in wildfire-affected soils is often not measured under fully saturated conditions because of water repellency, air entrapment in the affected soils, and other factors (Moody and others, 2016). As such, throughout this analysis, true saturated hydraulic conductivity, K_s, has been replaced with field saturated hydraulic conductivity, K_{fs}, to emphasize hydraulic conductivity values that have been determined under the less than fully saturated soil conditions that are usually present during postwildfire infiltration. Although K_{fs} and S can be determined by using the CI method, the method is not always conducive to detecting changes in infiltration rates and the corresponding changes in infiltration regimes that would limit the validity of the analysis (Vandervaere and others, 2000). For this reason, other methods can be used to verify specific subsets of the data that are valid for use with the CI method. These methods are discussed in the following sections.

Differentiated Linearization (DL)

If equation 3 is differentiated with respect to the square root of t ($t^{1/2}$), then changes in the infiltration rates determined by equation 3 are given by:

$$\frac{dI}{d(t^{1/2})} = S + 2Ct^{1/2} \quad (6)$$

The DL method is based on equation 6, which gives the rate of change of infiltration as a function of $t^{1/2}$. This relation is linear, and when the change in infiltration rate is plotted, deviations from a linear relation are easily identified. These nonlinear deviations can be indicative of discontinuities in infiltration rates, which in turn can be indicative of changes in infiltration regimes in the soil core. This ease in identifying changes by using the linear equation of the DL method makes the method very effective for determining the range of times for which infiltrometer data are valid for use in the SHP analysis, especially when compared to identifying changes with the quadratic equation of the CI method (Vandervaere and others, 2000).

Cumulative Linearization (CL)

In the laboratory processing of soil-core infiltrometer data, contact sand was used to provide hydraulic coupling between the infiltrometer base and the soil surface during wetting. Unfortunately, the contact sand also creates an artificial layer on the soil core, which may interfere with accurate estimation of SHPs. The influence of the contact sand layer may not be reliably identified with the CI and DL methods.

Similar to the linearization of the DL method, equation 3 can also be linearized by dividing by $t^{1/2}$, which gives the equation:

$$I / t^{1/2} = S + Ct^{1/2} \quad (7)$$

By using this equation, cumulative infiltration data can be plotted against $t^{1/2}$. Cook (2007) has shown that this linearization, referred to as cumulative linearization, can be effective in identifying the transition where infiltration across the core is controlled by the soil instead of the overlying contact sand. When used in combination with the CI and DL methods, the three methods together can be invaluable tools to identify the validity of the dataset when determining SHPs with laboratory infiltration measurements.

Using the Cumulative Infiltration, Differentiated Linearization, and Cumulative Linearization Methods to Determine Saturated Conductivity and Sorptivity

In this section, the use of the CI, DL, and CL methods together to determine hydraulic conductivity and sorptivity is illustrated. Laboratory data generated from sample LC–152–1 are used for the illustration.

Figure 7*A* was created by using the complete dataset from LC–152–1 and plotting the data with the quadratic equation 4 determined from the CI method. Although the graph appears linear, it is actually nonlinear, which is expected because it is a fitting of a quadratic equation, with the x^2 coefficient = -1.589×10^{-4} and the x coefficient = 4.483×10^{-2}. The negative x^2 coefficient would imply a negative K_{fs}, which is physically meaningless, and although the data appear to show two distinct subsets with two separate slopes, the equation nonetheless shows a good fit (R^2=0.936) across the complete dataset. As such, changes in infiltration rates are not completely obvious.

If the same complete dataset is plotted by using equation (6) of the DL method, graph *B* in figure 7 is created. In this graph, the linear relation between data points shows a distinct break in slope where the $t^{1/2}$ = 13, and this break suggests a change in infiltration regimes in the soil column at that time. However, if the complete dataset is also plotted with equation (7) of the CL method (fig. 8*A*), there is also an obvious break in the slope of the linear relation, but this break is at $t^{1/2}$ = 24, later than the break suggested by graph *B* with the DL method. With the additional insight gleaned from the application of the CL method, a new subset of data is created such that $t^{1/2}$ is greater than (>) 24, and this new subset is plotted with the DL method in figure 8*B*.

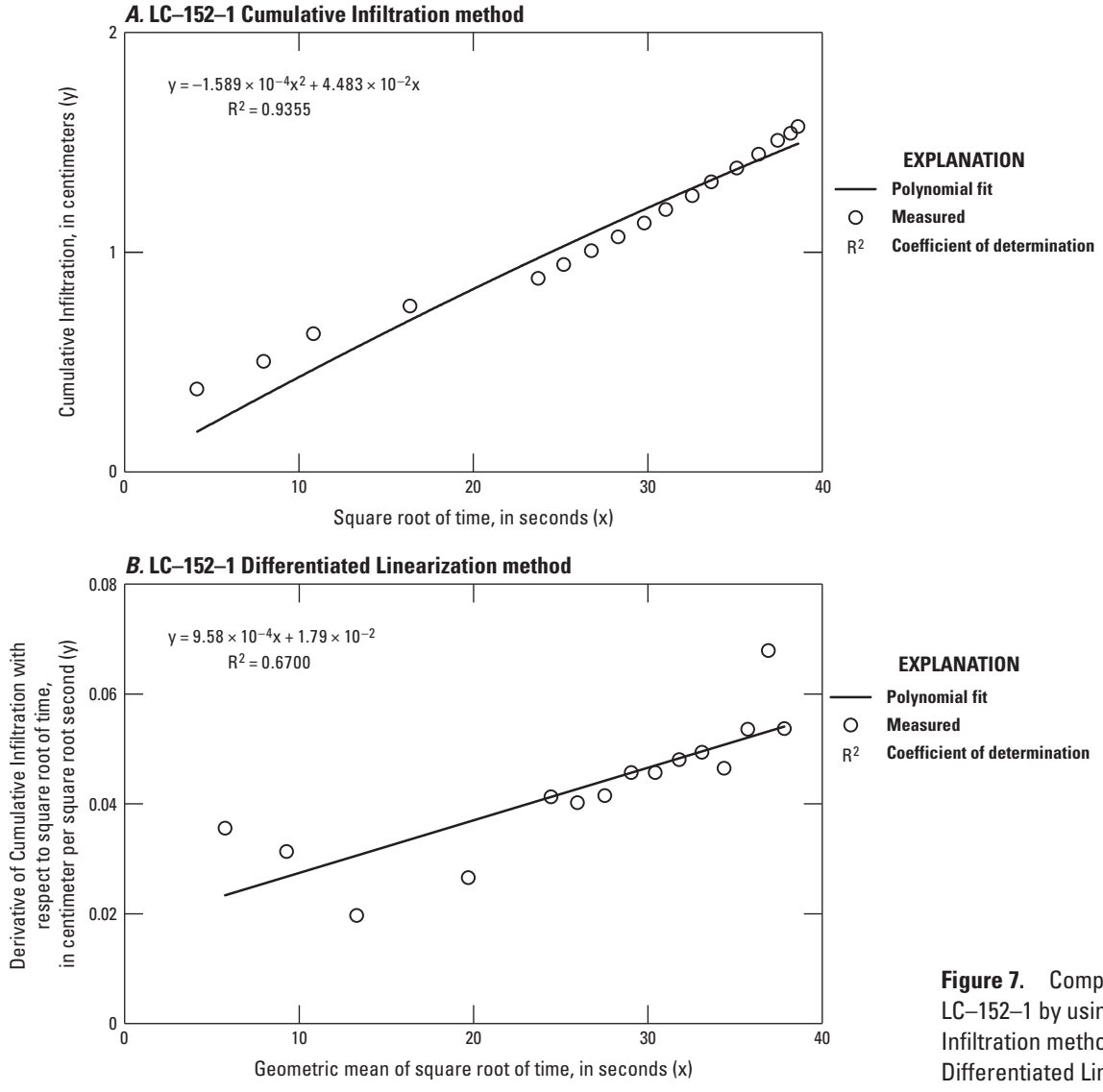

Figure 7. Complete datasets of LC–152–1 by using *A*, the Cumulative Infiltration method; and *B*, the Differentiated Linearization method.

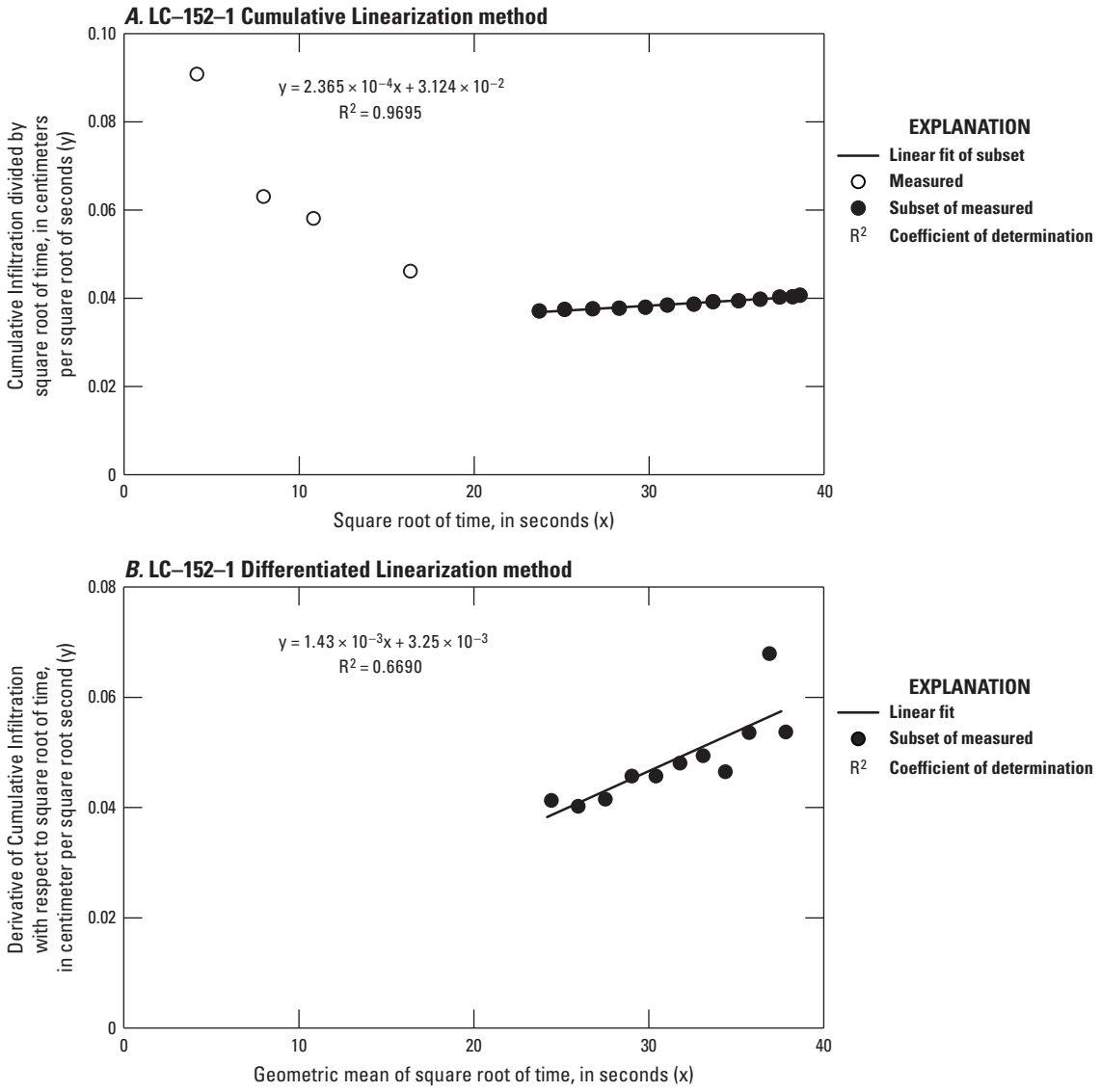

Figure 8. Data from sample LC–152–1 by using complete dataset and subset with the *A*, Cumulative Linearization method; and *B*, the Differentiated Linearization method.

Lastly, the new subset of data that has been determined with the DL and CL methods is used to create an additional graph by using the CI method and equation 4 (fig. 9). In this graph, the coefficient of the x term and the coefficient of the x^2 term are the equivalent of the S and C terms, respectively, in equation 4. The C coefficient can now be used with equation 5 to determine K_{fs}. In this example, S = 0.031 cm second$^{-1/2}$ ($s^{-1/2}$) and Kf_s = 0.00053 cm s^{-1}.

The methodology of comparing data using the CI, DL, and CL methods for each of the samples was similar to the methodology detailed above. A subset of data for each sample was selected such that K_{fs} and S were both greater than zero (when possible) and that the subset data did not contain obvious breaks in slope in the DL and CL methods. This optimized subset was then used to determine K_{fs} and S and this data-comparison methodology was used throughout the data processing and analysis portions of this report.

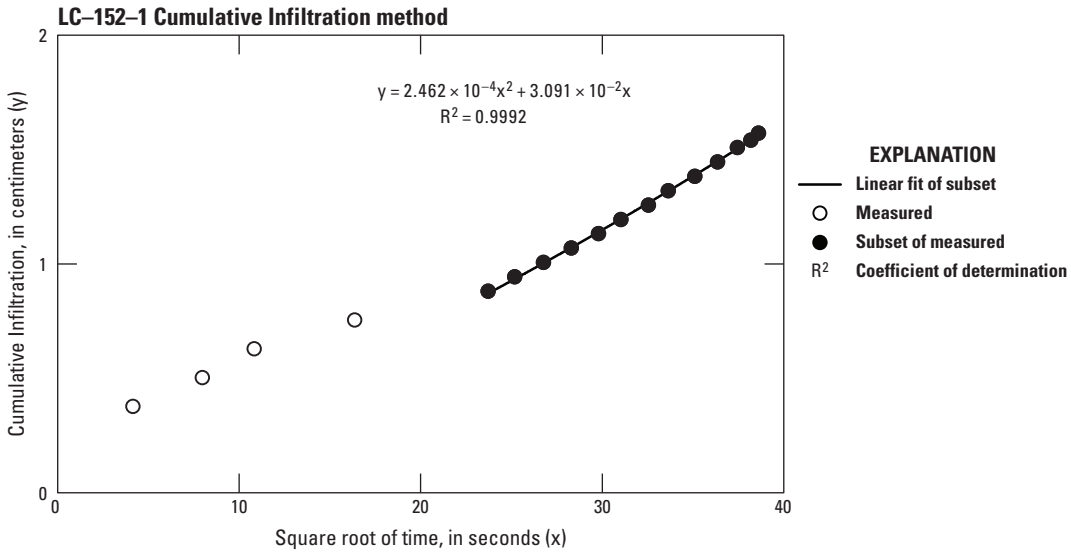

Figure 9. Complete dataset from LC–152–1 and the subset of data selected with the Differential Linearization and Cumulative Linearization methods.

Field Observations of Sampling Sites and Soil-Physical and Soil-Hydraulic Properties of Las Conchas Fire Samples

Field Observations of Sampling Sites

Physical descriptions of the sampling sites generally corresponded with the expectations based on burn-severity metrics (table 2). Sites LC–152 and LC–293 had little to no visible canopy effects from the fire and vigorous understory regrowth, which corresponds to the lower MTBS and BARC4 thematic class burn severity at these sites (table 1). Site LC–416 was more transitional, with some fine fuels present in the canopy and ample regrowth of grassy understory, but aspen regrowth was less dense. This finding is consistent with the transition to high severity for the MTBS and BARC4 thematic classes (table 1). The remaining sites are all listed as high severity for both the MTBS and BARC4 thematic classes, but the site observations (table 2) and the dNBR values (table 1) indicated a gradient of burn severity not captured by the thematic classes. For example, the LC–533, LC–618, and LC–802 sites still had some fine fuels present in the canopy, whereas LC–922 had very little fine fuel. The LC–533 and LC–618 sites had no evidence of rills, which are shallow channels cut into soil by flowing water, the LC–802 site had minor evidence of rills, and the LC–922 site had clearer remaining rill features. These differences suggested that greater erosion at the LC–802 and LC–922 sites may be reflective of greater soil burn severity, captured in the higher dNBR at the LC–802 and LC–922 sites.

Soil Physical Properties

Full Soil Cores (0–6 Centimeters)

For the full 6-cm length of soil core, the SPPs of initial and saturated volumetric soil-water content as well as bulk density do not show strong correlations with dNBR. For these cores, the SPPs between dNBR sites seem to vary more with location than with burn severity. For example, LC–533 and LC–618, although consecutively ranked in dNBR, have the lowest and highest saturated volumetric soil-water contents, respectively, of all the samples. These sites also have the highest and second lowest bulk densities, respectively, which suggests that saturated volumetric soil-water content at these sites may be driven by variations in soil texture rather than fire effects (fig. 10, table 3). There are some fire effects that are evident in the lower burn-severity sites LC–152, LC–293, and LC–416, which show increased saturated volumetric soil-water content and generally decreased bulk density values with increasing dNBR. These effects are not consistent, however, and the trends in volumetric soil-water content and bulk density values stop with dNBR greater than 416 (tables 3 and 5, fig. 10).

Table 2. Field observations of sampling sites in the 2011 Las Conchas wildfire burn scar, Jemez Mountains, north-central New Mexico.

Site Name	Description
LC–152	Cores were collected on 8 June 2015. There was no obvious surface ash but some cores have a layer of dark brown to red brown, with a black layer near the top of the core. Needle fall/litter layer was largely absent.
LC–293	Cores were collected on 8 June 2015. This site was heavily used by cattle recently. The surface had more grass than site 152 plus dandelions, mulleins, and fleabane
LC–416	Some fine fuels (needles and branches less than 1 cm) were present in the canopy. Aspens were less dense than LC533 or LC618. Soil surface was very grassy.
LC–533	Litter was thin and consists of partially decomposed aspen leaves (1–2 years old) with a thick aspen understory. Aspens were approximately 2.5 to 3.5 meters tall. Fine branches (branches less than 1 cm) of dead conifers were still on branches. Conifers were about 30 meters tall.
LC–618	Some fine branches (branches less than 1 cm) were present in the canopy. Aspen trees were approximately 3 years old and about 2.4 to 3.5 meters tall. Minor amount of 1–2 year old aspen litter was present on the ground surface as well as sparse moss. No evidence of rilling was observed.
LC–802	Some fine branches (branches less than 1 cm) were present in the canopy. Ground cover consisted of about 50% bare soil with no litter. A understory of sparse aspens about 1 meter tall was present as well as a plant identified by field staff as either Ribes or Physocarpus about 0.3 m tall. Some evidence of rilling at this site was observed.
LC–922	Very little fine fuel left in canopy. Ground surface did not have a litter layer. Some rills are still visible. Plant cover was mainly golden banner, dandelions, vetch, grass clumps, some moss and approximately 3-centimeter diameter rocks.

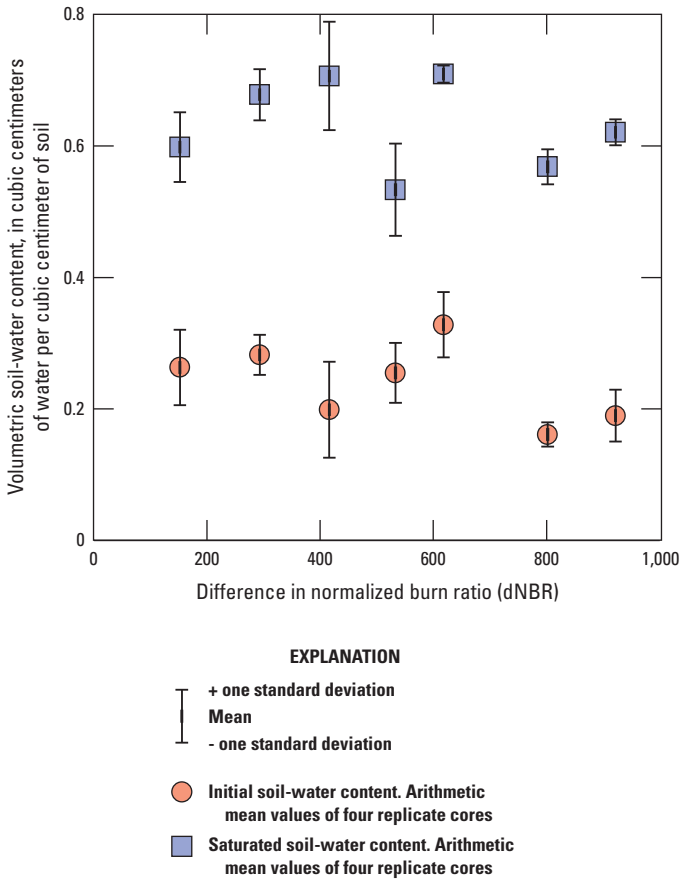

Figure 10. Initial (as sampled) and saturated volumetric soil-water content for the full 0–6 centimeter soil cores at the seven field sampling locations.

Table 3. Initial (θ_i) and saturated (θ_s) soil-water content and bulk density (ρ_b) for the soil-physical property cores within the perimeter of the 2011 Las Conchas Fire, Jemez Mountains, north-central New Mexico.

[All cores are 0–6 cm depth: σ, standard deviation; n, number of samples; $cm^3\ cm^{-3}$, cubic centimeters of water per cubic centimeters of soil; g cm–3, grams per cubic centimeters; ρ_b, bulk density]

Site name	Initial soil-water content (θ_i)		Saturated soil-water content (θ_s)		ρ_b		
	Mean ($cm^3\ cm^{-3}$)	σ ($cm^3\ cm^{-3}$)	Mean ($cm^3\ cm^{-3}$)	σ ($cm^3\ cm^{-3}$)	Mean ($g\ cm^{-3}$)	σ ($g\ cm^{-3}$)	n
LC–152	0.263	0.058	0.598	0.053	1.03	0.15	4
LC–293	0.282	0.031	0.678	0.039	0.78	0.12	4
LC–416	0.199	0.073	0.706	160.082	0.82	0.25	4
LC–533	0.255	0.045	0.533	0.070	1.32	0.17	4
LC–618	0.328	0.050	0.709	0.013	0.81	0.08	4
LC–802	0.161	0.018	0.568	0.027	1.30	0.12	4
LC–922	0.190	0.039	0.621	0.020	1.01	0.08	4

Measuring physical properties across the full 6 cm soil core, however, can mute evidence of fire effects because the measurements can average out the effects at depths that are either heavily affected or relatively unaffected by wildfire. For this reason, the samples were split further into 0–1, 1–3, and 3–6 cm depth intervals and analyzed individually at each new depth interval.

Soil Core Splits

The soil core splits into 0–1, 1–3, and 3–6 cm depth intervals show that fire effects on soil properties are concentrated in the top 1 cm. Soil samples from the top 1 cm show substantial fire effects on SPPs of loss on ignition and bulk density at dNBR values between 300 and 400 (table 4). The soil samples from the top 1 cm also show substantial fire effects on soil-particle size at dNBR values between 450 and 500 (table 5). All of these dNBR values approximately correspond to the MTBS thematic class break between moderate and high burn severity (dNBR equal to 380) and lie within the BARC4 thematic class for high severity. This would suggest that a threshold for substantial fire effects on soil properties in the top 1 cm of soil is greater than the range of 300 to 400 dNBR.

These burn-severity effects are supported by the bulk density results for 0–1 cm, with the lower severity sites (LC–152 and LC–293) having low bulk density, the LC–416 site having a slightly higher bulk density, and the higher severity sites (LC–533, LC–618, LC–802, and LC–922) having increased bulk density (table 4, fig. 11). The bulk density data support a threshold of dNBR between 300 and 400 for fire effects on soil physical properties, which corresponds to the MTBS thematic class break between moderate and high severity and the BARC4 thematic class for high severity. Similar burn-severity effects are seen in the loss on ignition (LOI) results for 0–1 cm. The LOI is greatest for the 0–1 cm depth for the lower severity sites LC–152 and LC–293 (fig. 12), is intermediate for the LC–416 site (which lies within a possible burn-severity threshold between 300 and 400 dNBR), and is low for the sites with higher dNBR (LC–533, LC–618, LC–802, and LC–922; table 4, fig. 12). Soil-particle size analysis showed that large organic particles (>0.25 mm) are a greater fraction, by mass, of the soil for the low severity sites (LC–152 and LC–293) for the 0–1 cm depth, reflecting the LOI results (table 5, fig. 13). Gravel (>2 mm) fractions for the 0–1 cm depth are low for the lower severity sites (LC–152 and LC–293), moderate for the moderate severity site (LC–416), and larger for the higher severity sites (LC–533, LC–618, LC–802, LC–922). The sand (2–0.063 mm) fraction is relatively constant across the sites, showing little correlation with dNBR for the 0–1 cm depth. Silt and clay (less than [<] 0.063 mm) fractions are greater for the lower severity sites LC–152 and LC–293, and site LC–416 for the 0–1 cm depth. The particle-size data from 0 to 1 cm support a threshold of dNBR between 450 and 500 for fire effects on particle size. This threshold is above the 300 to 400 dNBR threshold suggested by bulk density and LOI data and falls within the MTBS and BARC4 thematic classifications of high severity (table 5, fig. 13).

These wildfire effects on soil physical properties diminish with depth in the soil profile and are indistinguishable at depths of 1–3 and 3–6 cm below the surface. Bulk density shows much less correlation between dNBR and bulk density for the 1–3 and 3–6 cm depths than for the 0–1 cm depths (table 4, fig. 11). The LOI shows a similar trend as bulk density and shows no dependence on dNBR for the 1–3 and

Table 4. Bulk density (ρ_b) and loss on ignition (LOI) results for the soil-physical property cores for splits from 0 to 1, 1 to 3, and 3 to 6 centimeter depths within the perimeter of the 2011 Las Conchas Fire, Jemez Mountains, north-central New Mexico.

[σ, standard deviation; n, number of samples; g cm-3, grams per cubic centimeters; cm, centimeters; LOI, Loss on ignition in percent; %, percentage; ρ_b, bulk density]

Site name	0–1 cm depth						1–3 cm depth						3–6 cm depth					
	ρ_b			LOI			ρ_b			LOI			ρ_b			LOI		
	Mean (g cm–3)	σ (g cm–3)	n	Mean (%)	σ (%)	n	Mean (g cm–3)	σ (g cm–3)	n	Mean (%)	σ (%)	n	Mean (g cm–3)	σ (g cm–3)	n	Mean (%)	σ (%)	n
LC–152	0.67	0.33	4	30.5	26.0	4	0.94	0.15	4	8.2	1.5	4	1.21	0.23	4	6.5	1.0	4
LC–293	0.31	0.02	3	43.3	18.0	3	0.90	0.51	3	14.1	6.1	3	0.90	0.10	3	8.7	1.2	3
LC–416	0.77	0.44	4	16.8	11.5	4	0.79	0.28	4	13.0	7.0	4	0.86	0.23	4	13.4	7.7	4
LC–533	1.14	0.40	4	7.7	3.2	4	1.08	0.10	4	7.1	1.8	4	1.54	0.23	4	6.4	1.1	4
LC–618	0.88	0.26	3	12.1	3.0	3	0.62	0.09	3	10.3	2.0	3	0.91	0.10	3	8.9	1.0	3
LC–802	1.66	0.39	4	6.0	0.7	4	1.34	0.15	4	5.0	0.8	4	1.16	0.16	4	6.2	1.5	4
LC–922	1.43	0.22	3	8.4	2.5	3	0.85	0.06	3	8.9	1.6	3	1.16	0.04	4	6.3	0.5	4

3–6 cm depths (fig. 12, table 4). The large organic fraction, by mass, from the particle-size analysis is low across the full spectrum of dNBR, indicating that organic matter is contained primarily in the top 1 cm of the soils at these sites (table 5, figs. 13–15). The fraction of gravel for the 1–3 cm depths is lower for the LC–152 and LC–416 sites but higher for the LC–293, LC–533, LC–618, LC–802, and LC–922 sites, which suggests some dependence on dNBR but less than the 0–1 cm depth. Sand fractions are similar across the sites, showing little correlation with dNBR for the 1–3 cm depth. The fractions of silt and clay are greater for the lower severity sites LC–152 and LC–293, and LC–416 for the 1–3 cm depth. Similar to the 0–1 cm depth, the particle-size data support a dNBR threshold of between 450 and 500 (table 5, figs. 14–15).

Only three samples were excluded, either entirely or in part, from the analyses. Sample LC-293-11 was spilled after the full 6 cm soil core analysis, and for that reason this sample does not have split soil core data. Sample LC-618-12 spilled during the 1-3 cm split, and this split was also removed from the analysis. Lastly, LC-922-14 had sieving problems during the 1-3 cm split and was consequently analyzed for the 0-3 and 3-6 cm splits only. No samples, other than those that were spilled, exceeded the 5 percent error tolerance discussed in the "Methods and Approach" section.

Soil Hydraulic Properties

Field-Saturated Hydraulic Conductivity, K_{fs}

The SHP K_{fs} was not inversely correlated with burn severity. The K_{fs} values did not depend on dNBR (tables 6 and 7, fig. 16), and no transitions corresponding to MTBS or BARC4 thematic class thresholds (table 1) were evident. The values of K_{fs} ranged over approximately two orders of magnitude (tables 6 and 7), from 10^{-1} to 10^{-3} cm s^{-1}, regardless of dNBR. The highest burn-severity site, LC–922, did appear to have a slightly smaller range of K_{fs} values, from 10^{-1} to 10^{-2} cm s^{-1} (fig. 16). The values of K_{fs} did not appear to change depending on the method of infiltrometer data analysis (that is, CI compared to CL versus DL method) (tables 6 and 7); however, some evidence of heterogeneity and the use of contact sand indicate that the DL results are the most appropriate for interpretation because the DL method is best suited for this situation (Vandervaere and others, 2000). The number of samples with viable infiltrometer results (that is, K_{fs} and S both > 0) were approximately the same regardless of burn severity, although site LC–533 had fewer viable infiltrometer results than the other sites (tables 6 and 7). An exponential regression through the geometric means of the DL method for K_{fs} values suggests a slightly increasing trend for K_{fs} with increasing dNBR, which was contrary to expectations (fig. 16). The small coefficient of determination (R^2) value of 0.17 for the regression and large spread in values, based on ± one standard deviation, suggests there is no strong relation between K_{fs} and dNBR or MTBS/ BARC4 thematic classes at this site 4 years after the wildfire (fig. 16*A*). The F-test p-value for the geometric mean of K_{fs} regressed against dNBR is 0.233, which exceeds the threshold p-value of 0.05; therefore, the trends in the regressions are not indicated to be significant within the assumptions of the statistical test.

Table 5. Soil particle size analysis from within the perimeter of the 2011 Las Conchas Fire, Jemez Mountains, north-central New Mexico.

[mm is millimeter; >, greater than; %, percentage; gravel is > 2 mm; sand is 2–0.063 mm; silt and clay are <0.063 mm; large organics are > 0.250 mm; cm is centimeter; g is grams]

Sample name	depth (cm)	>8 mm (g)	8–4 mm (g)	4–2 mm (g)	2–1 mm (g)	1–0.5 mm (g)	0.500–0.250 mm (g)	0.250–0.125 mm (g)	0.125–0.063 mm (g)	<0.063 mm (g)	Large organics (g)	Gravel (%)	Sand (%)	Silt and clay (%)	Large organics (%)
LC–152–11	0–1	0.000	0.000	0.000	0.007	0.008	0.191	0.182	0.322	0.756	4.467	0.0	12.0	12.7	75.3
	1–3	0.000	2.086	1.359	0.865	0.781	1.169	1.742	4.758	13.150	0.302	13.1	35.5	50.2	1.2
	3–6	2.011	1.786	3.754	3.163	3.262	3.678	4.705	8.732	13.943	0.117	16.7	52.1	30.9	0.3
LC–152–12	0–1	0.000	0.726	0.329	0.502	0.967	1.975	2.014	4.466	4.054	1.131	6.5	61.4	25.1	7.0
	1–3	0.000	0.849	2.037	2.190	2.788	3.987	4.228	8.693	9.489	0.359	8.3	63.2	27.4	1.0
	3–6	0.584	1.231	2.748	4.385	7.554	6.468	5.768	8.031	11.246	0.033	9.5	67.0	23.4	0.1
LC–152–13	0–1	0.000	1.060	0.596	0.353	0.375	0.353	0.420	0.910	1.129	1.447	24.9	36.3	17.0	21.8
	1–3	0.000	5.563	2.267	2.245	2.057	2.348	3.444	5.512	7.407	0.082	25.3	50.5	24.0	0.3
	3–6	10.113	10.639	4.837	3.950	3.335	4.400	4.510	6.416	7.453	0.051	45.9	40.6	13.4	0.1
LC–152–14	0–1	0.000	0.000	0.306	0.689	0.882	0.950	1.590	2.710	5.996	1.661	2.1	46.1	40.6	11.2
	1–3	0.000	1.155	2.876	1.411	2.133	2.289	2.432	4.222	9.939	0.203	15.1	46.8	37.3	0.8
	3–6	0.000	2.690	2.374	2.484	3.203	3.117	2.950	5.284	8.304	0.216	16.5	55.6	27.1	0.7
LC–293–11	[a]0–6	7.906	3.905	6.706	3.415	3.406	2.812	3.791	10.862	27.224	0.870	26.1	34.3	38.4	1.2
LC–293–12	0–1	0.000	0.460	0.000	0.007	0.006	0.063	0.088	0.276	0.756	3.322	9.2	8.8	15.2	66.7
	1–3	2.199	1.083	1.024	0.580	0.410	0.761	0.885	1.594	6.172	0.728	27.9	27.4	40.0	4.7
	3–6	2.652	3.013	2.536	1.515	1.236	1.783	1.831	3.287	9.635	1.861	27.9	32.9	32.8	6.3
LC–293–13	0–1	0.000	0.516	0.258	0.257	0.258	0.277	0.229	0.446	2.256	0.964	14.2	26.9	41.3	17.7
	1–3	40.337	1.464	1.100	0.533	0.238	0.236	0.320	0.720	3.533	0.110	88.3	4.2	7.3	0.2
	3–6	4.050	2.090	1.272	0.824	0.623	0.693	0.554	1.999	6.026	0.030	40.8	25.8	33.2	0.2
LC–293–14	0–1	0.000	0.000	0.000	0.341	0.893	0.696	0.621	0.795	1.347	0.247	0.0	67.7	27.3	5.0
	1–3	2.607	1.699	1.760	1.135	0.825	0.762	1.554	3.753	11.307	0.200	23.7	31.4	44.2	0.8
	3–6	3.625	3.146	4.464	2.916	3.407	3.782	3.073	3.744	8.873	0.321	30.1	45.3	23.8	0.9
LC–416–11	0–1	0.000	0.195	0.147	0.073	0.114	0.130	0.353	0.515	1.686	0.293	9.8	33.8	48.1	8.4
	1–3	0.000	0.711	0.507	0.397	0.376	0.906	1.362	3.653	4.868	0.954	8.9	48.7	35.4	6.9
	3–6	0.000	0.110	0.128	0.516	1.803	3.202	4.738	6.358	3.987	1.478	1.1	74.4	17.9	6.6
LC–416–12	0–1	3.813	3.266	1.067	0.653	0.587	0.633	0.937	2.720	4.964	0.020	43.7	29.6	26.6	0.1
	1–3	0.000	3.990	2.982	1.985	1.465	1.756	3.110	5.708	8.165	0.022	23.9	48.1	28.0	0.1
	3–6	5.266	3.478	2.664	2.641	4.396	4.146	3.231	3.843	3.482	0.105	34.3	54.9	10.5	0.3
LC–416–13	0–1	1.105	0.938	0.788	0.703	0.845	1.582	2.133	3.824	6.197	0.180	15.5	49.7	33.9	1.0
	1–3	6.452	1.306	1.071	0.983	2.380	3.620	3.896	3.641	1.550	0.571	34.7	57.0	6.1	2.2

Table 5. Soil particle size analysis from within the perimeter of the 2011 Las Conchas Fire, Jemez Mountains, north-central New Mexico.—Continued

[mm is millimeter; >, greater than; %, percentage; gravel is > 2 mm; sand is 2–0.063 mm; silt and clay are <0.063 mm; large organics are > 0.250 mm; cm is centimeter; g is grams]

Sample name	depth (cm)	>8 mm (g)	8–4 mm (g)	4–2 mm (g)	2–1 mm (g)	1–0.5 mm (g)	0.500–0.250 mm (g)	0.250–0.125 mm (g)	0.125–0.063 mm (g)	<0.063 mm (g)	Large organics (g)	Gravel (%)	Sand (%)	Silt and clay (%)	Large organics (%)
	3–6	0.000	0.192	0.744	1.494	5.578	5.974	5.113	5.998	4.369	0.560	3.1	80.5	14.6	1.9
LC–416–14	0–1	0.000	1.775	0.916	0.736	1.088	1.081	0.956	1.148	2.259	0.013	27.0	50.2	22.7	0.1
	1–3	0.000	3.859	3.782	2.567	4.398	5.700	4.162	4.916	6.902	0.000	21.1	59.9	19.0	0.0
	3–6	0.000	3.096	6.793	3.066	5.923	5.783	4.448	4.711	5.760	1.503	24.1	58.3	14.0	3.7
LC–533–11	0–1	2.190	4.657	3.637	2.156	1.774	1.082	0.535	0.581	0.083	0.049	62.6	36.6	0.5	0.3
	1–3	2.555	6.856	9.141	7.072	5.316	3.503	2.055	1.769	2.075	0.024	46.0	48.8	5.1	0.1
	3–6	0.000	10.107	17.348	15.746	9.890	6.009	3.901	3.990	5.153	0.147	38.0	54.7	7.1	0.2
LC–533–12	0–1	1.510	4.557	4.888	3.792	2.892	1.410	0.730	0.635	0.920	0.340	50.5	43.6	4.2	1.6
	1–3	3.051	8.006	7.879	6.633	4.173	2.119	1.113	0.819	1.104	0.394	53.7	42.1	3.1	1.1
	3–6	4.359	6.282	9.630	12.598	8.486	5.274	3.151	2.413	2.798	0.225	36.7	57.8	5.1	0.4
LC–533–13	0–1	0.838	1.629	2.371	1.346	1.724	1.061	0.456	0.319	0.453	0.519	45.1	45.8	4.2	4.8
	1–3	0.000	7.938	15.719	2.102	2.491	1.321	0.702	0.569	0.728	0.464	73.8	22.4	2.3	1.4
	3–6	1.924	15.685	15.219	7.225	5.217	2.845	1.809	1.824	2.753	0.360	59.8	34.5	5.0	0.7
LC–533–14	0–1	4.803	4.585	4.542	4.573	2.570	1.344	0.842	0.805	1.306	0.890	53.0	38.6	5.0	3.4
	1–3	2.053	2.150	11.998	6.590	4.979	2.638	1.331	1.509	2.509	0.753	44.4	46.7	6.9	2.1
	3–6	4.723	8.732	16.837	11.955	7.833	4.884	3.091	2.685	4.043	0.412	46.5	46.7	6.2	0.6
LC–618–11	0–1	0.000	3.386	2.743	1.714	2.240	1.404	0.823	0.919	1.747	0.607	39.3	45.6	11.2	3.9
	1–3	0.986	2.719	9.113	1.962	2.917	1.453	0.913	1.095	2.685	0.234	53.2	34.6	11.2	1.0
	3–6	4.032	3.578	5.859	5.500	3.909	2.055	1.400	1.730	3.909	0.481	41.5	45.0	12.0	1.5
LC–618–12	0–1	3.481	1.362	1.892	0.892	0.610	0.695	0.867	1.518	2.816	0.487	46.1	31.3	19.3	3.3
	[a]1–3	2.324	4.100	2.011	1.135	0.577	0.272	0.532	2.318	4.122	0.272	47.8	27.4	23.3	1.5
	3–6	3.167	4.646	3.726	2.249	1.984	2.741	3.039	5.282	11.274	0.581	29.8	39.5	29.1	1.5
LC–618–13	0–1	0.000	4.835	2.666	1.421	1.600	1.258	1.136	1.694	3.692	0.960	38.9	36.9	19.2	5.0
	1–3	1.585	1.320	1.882	1.481	1.907	1.277	1.333	1.830	4.169	0.757	27.3	44.6	23.8	4.3
	3–6	2.009	6.250	4.886	3.697	4.121	3.170	2.587	3.613	8.022	0.855	33.5	43.8	20.5	2.2
LC–618–14	0–1	0.717	1.792	1.629	0.476	0.603	0.508	0.391	0.562	1.165	1.191	45.8	28.1	12.9	13.2
	1–3	0.336	2.252	2.689	2.812	3.401	2.140	1.371	1.629	3.398	0.477	25.7	55.4	16.6	2.3
	3–6	0.412	1.161	3.063	2.907	3.006	2.199	1.725	2.117	3.596	0.305	22.6	58.3	17.5	1.5
LC–802–11	0–1	2.915	1.945	4.351	1.529	1.788	1.938	1.666	1.683	2.973	1.129	42.0	39.3	13.6	5.2
	1–3	4.789	9.534	8.324	5.082	5.383	3.849	3.275	2.944	4.668	2.290	45.2	41.0	9.3	4.6
	3–6	2.413	4.635	1.914	1.479	2.683	3.496	2.990	3.036	4.757	0.346	32.3	49.3	17.1	1.2

Table 5. Soil particle size analysis from within the perimeter of the 2011 Las Conchas Fire, Jemez Mountains, north-central New Mexico.—Continued

[mm is millimeter; >, greater than; %, percentage; gravel is > 2 mm; sand is 2–0.063 mm; silt and clay are <0.063 mm; large organics are > 0.250 mm; cm is centimeter; g is grams]

Sample name	depth (cm)	>8 mm (g)	8–4 mm (g)	4–2 mm (g)	2–1 mm (g)	1–0.5 mm (g)	0.500–0.250 mm (g)	0.250–0.125 mm (g)	0.125–0.063 mm (g)	<0.063 mm (g)	Large organics (g)	Gravel (%)	Sand (%)	Silt and clay (%)	Large organics (%)
LC–802–12	0–1	1.962	5.137	5.327	2.606	3.037	5.097	3.673	3.322	4.916	1.687	33.8	48.2	13.4	4.6
	1–3	0.000	6.123	7.298	2.113	3.116	4.758	3.453	2.996	4.030	0.695	38.8	47.5	11.7	2.0
	3–6	1.299	3.531	5.807	4.042	5.221	6.274	4.858	4.356	5.973	1.714	24.7	57.5	13.9	4.0
LC–802–13	0–1	14.924	8.116	2.992	1.444	1.319	1.353	1.635	1.697	2.219	1.629	69.7	20.0	5.9	4.4
	1–3	4.746	8.653	7.621	2.454	3.476	3.534	2.699	2.767	3.678	1.275	51.4	36.5	9.0	3.1
	3–6	3.353	6.051	4.750	3.199	5.216	5.058	3.817	4.092	5.569	0.758	33.8	51.1	13.3	1.8
LC–802–14	0–1	6.024	2.949	2.979	2.586	2.534	2.273	2.124	1.635	1.757	1.201	45.9	42.8	6.7	4.6
	1–3	2.844	4.193	5.180	4.101	5.060	5.179	4.476	3.616	3.361	1.647	30.8	56.6	8.5	4.2
	3–6	1.502	2.126	4.359	3.168	4.206	4.402	4.020	4.119	3.480	1.171	24.5	61.2	10.7	3.6
LC–922–11	0–1	1.326	2.112	1.133	1.097	2.299	3.322	2.387	3.577	6.390	1.131	18.5	51.2	25.8	4.6
	1–3	1.995	1.970	2.210	2.240	4.262	2.952	2.545	3.321	6.013	1.708	21.1	52.4	20.6	5.8
	3–6	6.172	7.832	3.557	1.661	2.794	2.236	1.872	2.855	4.412	0.363	52.0	33.8	13.1	1.1
LC–922–12	0–1	2.551	3.000	1.172	0.542	0.616	1.023	1.086	1.618	3.281	0.671	43.2	31.4	21.1	4.3
	1–3	0.968	2.874	3.048	1.529	2.459	3.706	3.002	3.808	6.669	1.005	23.7	49.9	22.9	3.5
	3–6	3.643	2.184	3.046	1.893	3.359	3.231	2.631	3.971	5.135	0.596	29.9	50.8	17.3	2.0
LC–922–13	0–1	1.555	4.957	1.939	1.092	1.093	1.447	1.366	1.942	3.134	0.829	43.7	35.9	16.2	4.3
	1–3	0.000	1.413	0.914	2.477	4.001	3.697	2.316	3.242	6.101	1.236	9.2	61.9	24.0	4.9
	3–6	3.257	2.248	3.631	3.676	4.225	2.813	1.915	2.354	3.974	0.332	32.1	52.7	14.0	1.2
LC–922–14	0–3	0.000	5.304	5.214	2.193	3.849	4.067	2.907	3.194	5.342	2.380	30.5	47.1	15.5	6.9
	3–6	0.534	1.750	3.283	3.762	5.052	4.154	3.168	3.961	5.647	0.463	17.5	63.2	17.8	1.5

[a]Sample spilled during sieving.

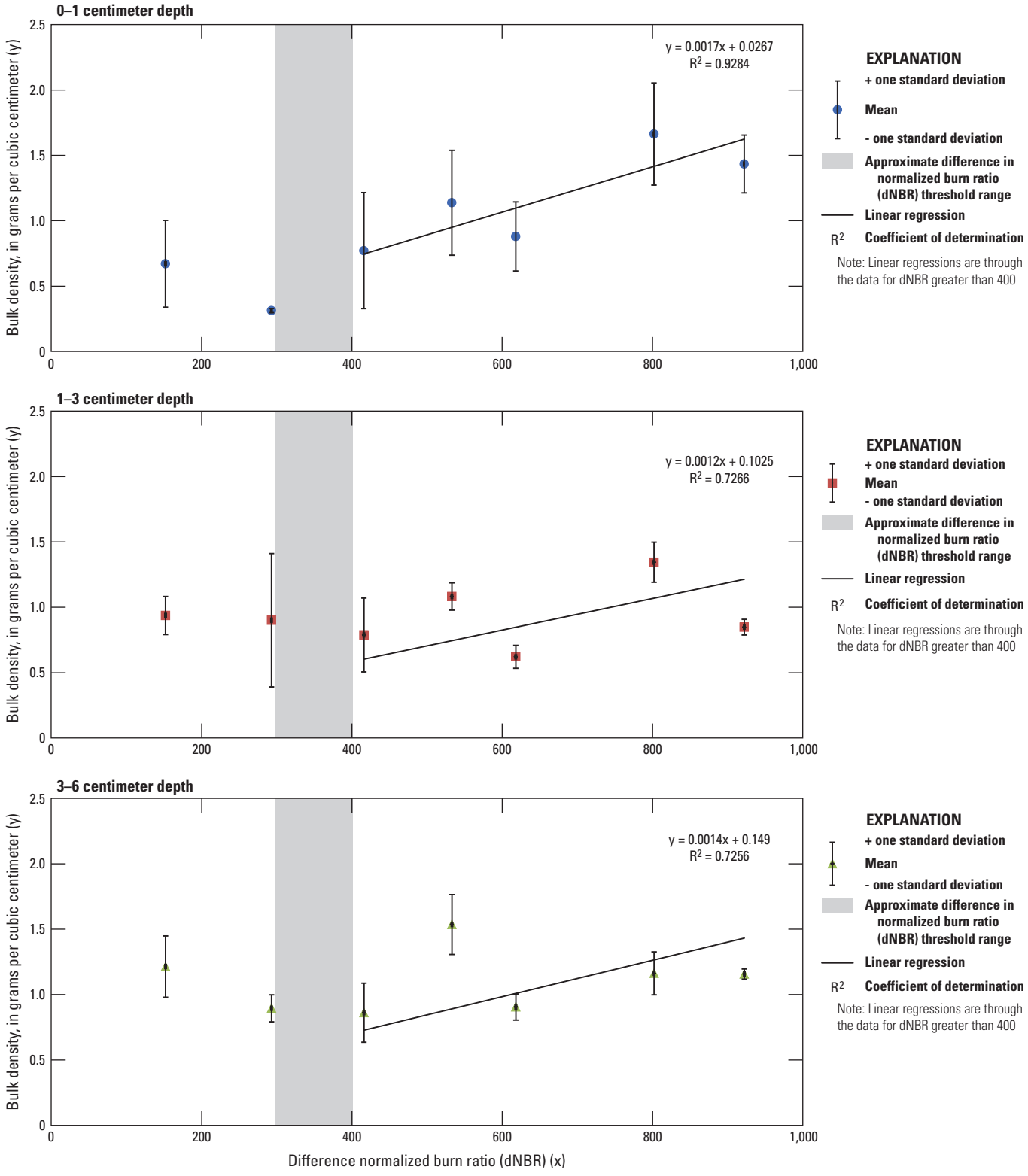

Figure 11. Bulk density for three splits of the soil cores corresponding to 0–1, 1–3, and 3–6 centimeter depths for the seven sampling locations. Points are arithmetic mean values of four replicate samples and error bars are ± one standard deviation.

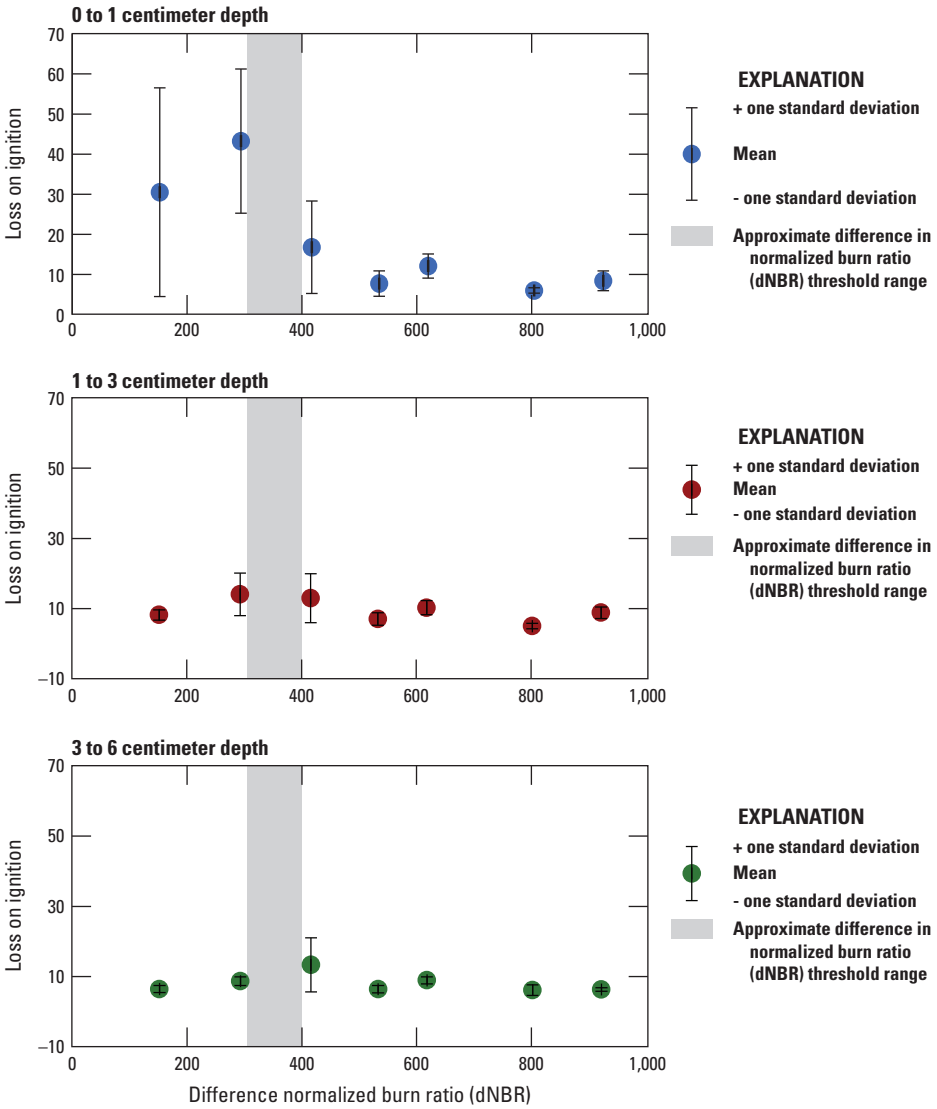

Figure 12. Loss on Ignition (LOI), which is a measure of soil organic matter, for three splits of the soil cores corresponding to 0–1, 1–3, and 3–6 centimeter depths at the seven sampling locations.

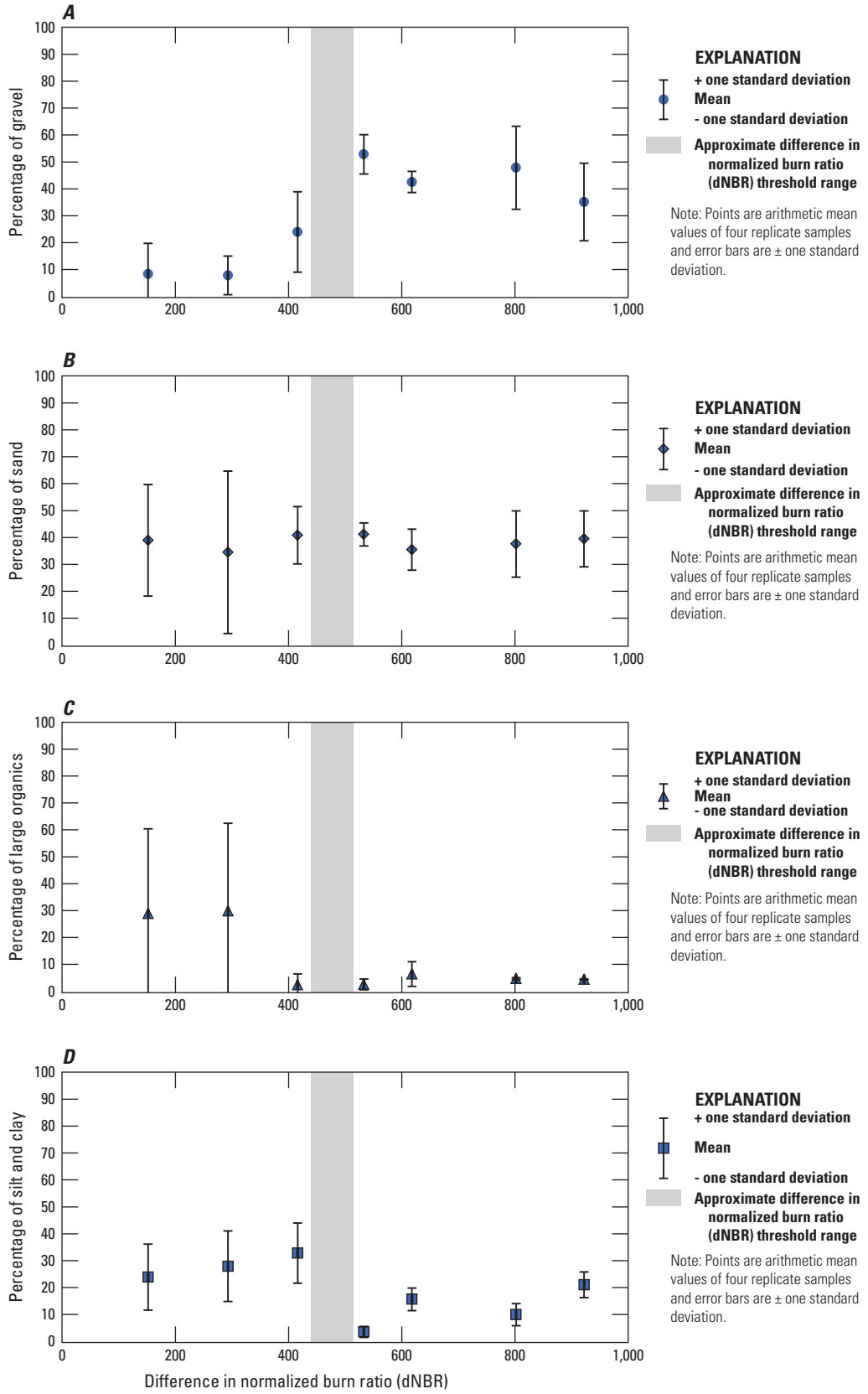

Figure 13. Soil particle size percentages by mass of *A*, gravel; *B*, sand; *C*, organic particles greater than 0.25 millimeters; and *D*, the combined silt and clay fraction for 0–1 centimeter depth for the seven sampling locations.

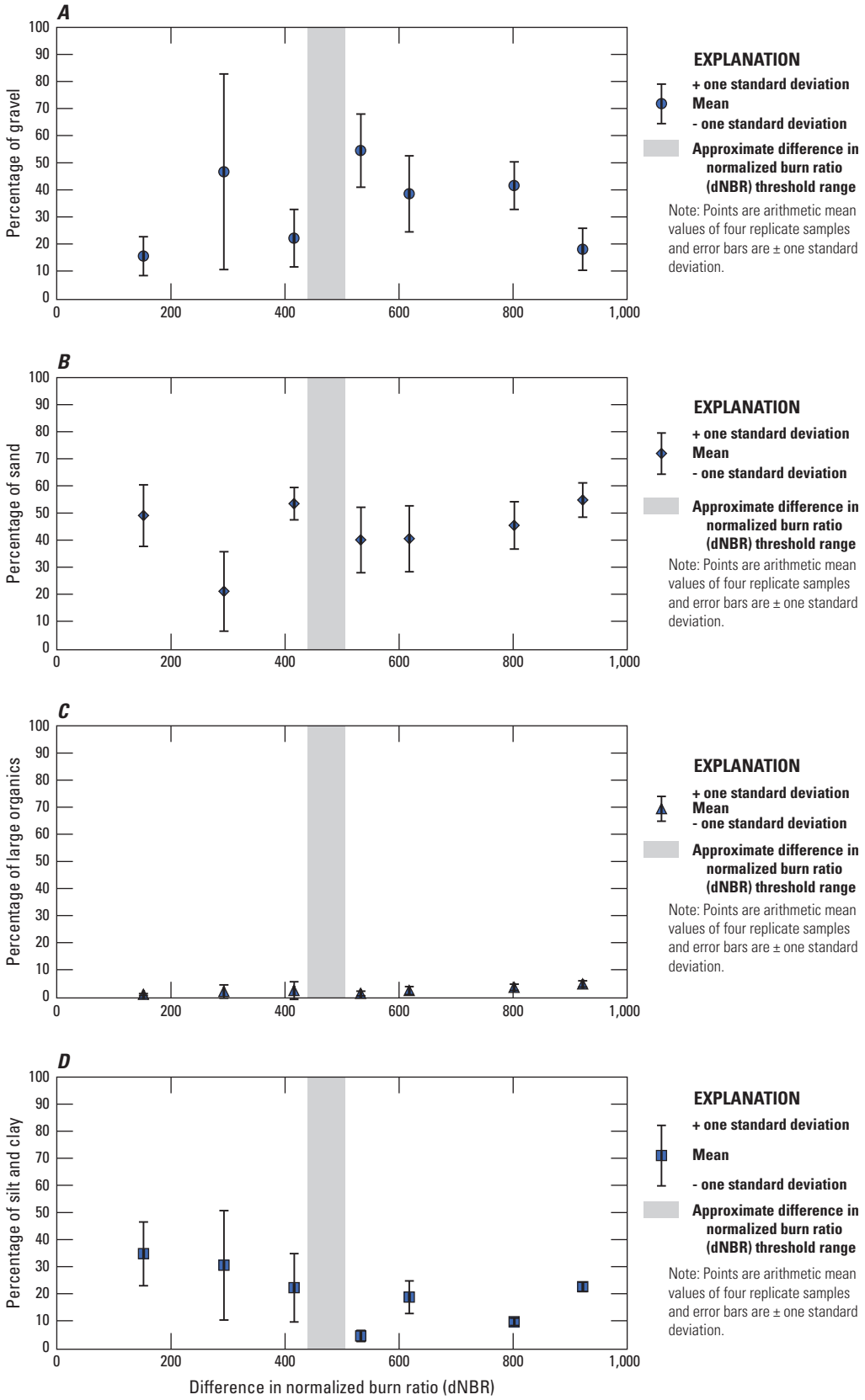

Figure 14. Soil particle size percentages by mass of *A*, gravel; *B*, sand; *C*, organic particles greater than 0.25 millimeter; and *D*, the combined silt and clay fraction for 1–3 centimeter depth for the seven sampling locations.

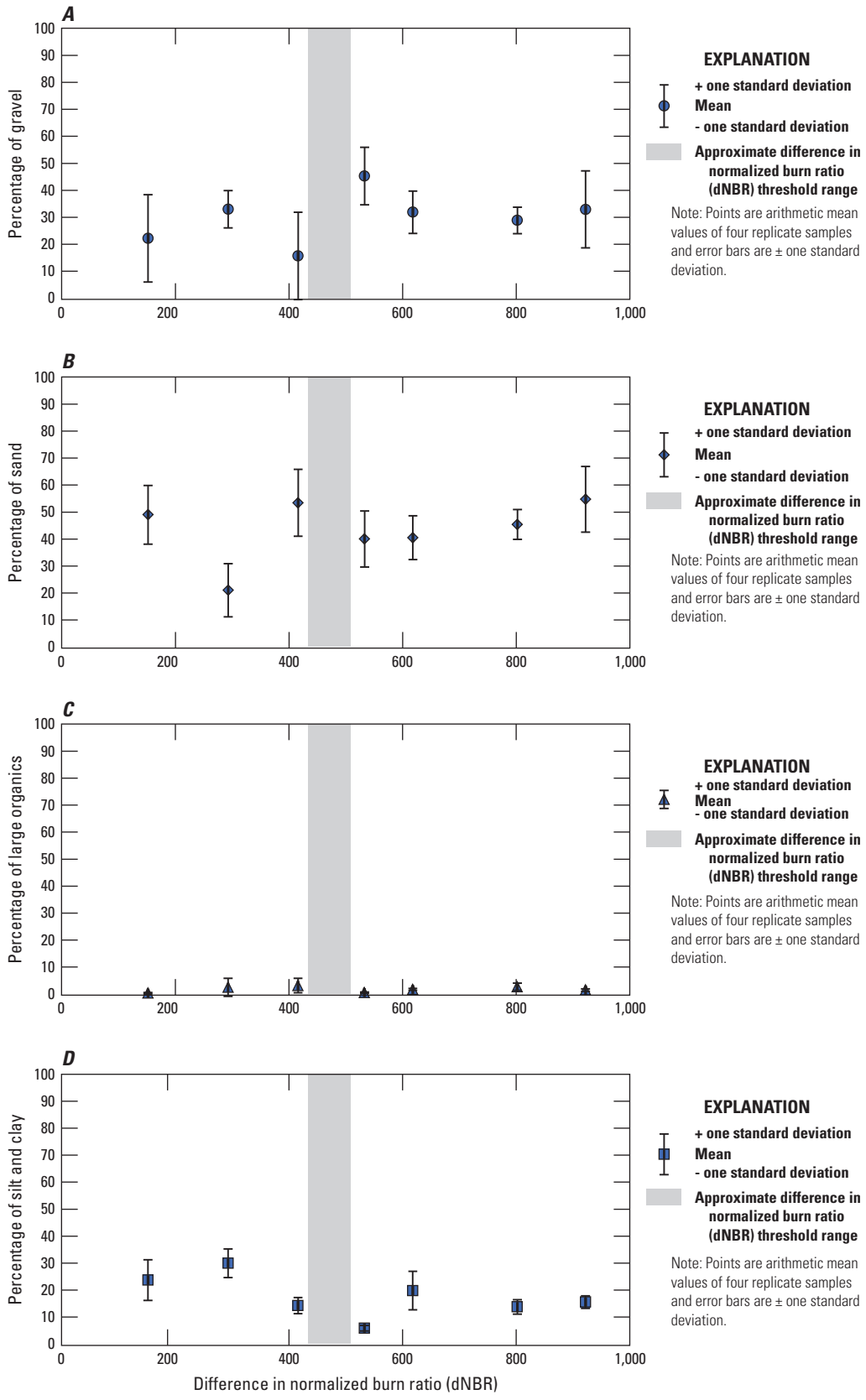

Figure 15. Soil particle size percentages by mass of *A*, gravel; *B*, sand; *C*, organic particles greater than 0.25 millimeters; and *D*, the combined silt and clay fraction for 3–6 centimeter depth for the seven sampling locations.

Table 6. Measured values from tension infiltrometer tests on intact core samples.

[The core identification begins with the site name, then the sample number. For example, core ID 152–4 is the fourth core from site LC–152; three analysis methods used from Vandervaere and others (2000) are the Cumulative Infiltration (CI), Cumulative Linearization (CL), and Differentiated Linearization (DL) methods ; Bolded text denotes if either field-saturated hydraulic conductivity (K_{fs}) or sorptivity (S) was a negative value, which indicates that neither the Kfs nor the S values were used in further analysis; cm s^{-1}, centimeters per second; cm $s^{-0.5}$, centimeters per square root of second; (-), dimensionless; R^2, coefficient of determination; dNBR, difference in Normalized Burn Ratio]

Sample name	K_{fs} (cm s^{-1})	S (cm $s^{-0.5}$)	R^2 (-)	dNBR (-)	Method
LC–152–1	5.28×10^{-4}	3.09×10^{-2}	1.00	152	CI
LC–152–1	5.07×10^{-4}	3.12×10^{-2}	0.97	152	CL
LC–152–1	1.53×10^{-3}	3.25×10^{-3}	0.67	152	DL
LC–152–2	***-3.20×10^{-4}***	***4.14×10^{-2}***	0.98	152	CI
LC–152–2	***-9.58×10^{-3}***	***4.71×10^{-2}***	0.44	152	CL
LC–152–2	1.70×10^{-3}	1.06×10^{-2}	0.68	152	DL
LC–152–3	***-7.62×10^{-4}***	***4.74×10^{-2}***	0.98	152	CI
LC–152–3	***-9.00×10^{-4}***	***4.93×10^{-2}***	0.89	152	CL
LC–152–3	1.11×10^{-3}	2.65×10^{-3}	0.90	152	DL
LC–152–4	3.89×10^{-2}	6.66×10^{-2}	1.00	152	CI
LC–152–4	3.74×10^{-2}	7.06×10^{-2}	0.99	152	CL
LC–152–4	4.00×10^{-2}	7.20×10^{-2}	0.93	152	DL
LC–152–5	6.64×10^{-4}	3.31×10^{-2}	0.99	152	CI
LC–152–5	4.32×10^{-4}	3.65×10^{-2}	0.40	152	CL
LC–152–5	2.05×10^{-3}	3.93×10^{-4}	0.68	152	DL
LC–152–6	1.86×10^{-2}	1.47×10^{-2}	1.00	152	CI
LC–152–6	1.50×10^{-2}	3.48×10^{-2}	0.91	152	CL
LC–152–6	***2.55×10^{-2}***	***-4.07×10^{-2}***	0.95	152	DL
LC–152–7	***4.03×10^{-2}***	***-3.44×10^{-3}***	0.98	152	CI
LC–152–7	3.38×10^{-2}	2.02×10^{-2}	0.89	152	CL
LC–152–7	4.09×10^{-2}	5.00×10^{-3}	0.27	152	DL
LC–152–8	***-1.88×10^{-3}***	***6.82×10^{-2}***	0.97	152	CI
LC–152–8	***-2.59×10^{-3}***	***7.47×10^{-2}***	0.85	152	CL
LC–152–8	9.33×10^{-4}	2.39×10^{-2}	0.88	152	DL
LC–152–9	1.99×10^{-2}	7.53×10^{-2}	1.00	152	CI
LC–152–9	2.01×10^{-2}	7.44×10^{-2}	0.98	152	CL
LC–152–9	2.19×10^{-2}	6.35×10^{-2}	0.46	152	DL
LC–152–10	2.78×10^{-3}	2.52×10^{-2}	1.00	152	CI
LC–152–10	2.79×10^{-3}	2.51×10^{-2}	0.98	152	CL
LC–152–10	4.36×10^{-3}	8.72×10^{-3}	0.71	152	DL
LC–293–1	***-9.77×10^{-4}***	***4.99×10^{-2}***	0.87	293	CI
LC–293–1	***-1.55×10^{-3}***	***6.10×10^{-2}***	0.85	293	CL
LC–293–1	2.54×10^{-4}	1.28×10^{-2}	0.38	293	DL
LC–293–2	***5.34×10^{-2}***	***-8.92×10^{-2}***	1.00	293	CI
LC–293–2	5.26×10^{-2}	2.80×10^{-3}	0.99	293	CL
LC–293–2	5.40×10^{-2}	1.09×10^{-2}	0.70	293	DL
LC–293–3	3.60×10^{-3}	1.36×10^{-2}	0.99	293	CI
LC–293–3	1.16×10^{-3}	3.77×10^{-2}	0.17	293	CL
LC–293–3	***4.71×10^{-3}***	***-2.73×10^{-3}***	0.99	293	DL
LC–293–4	2.63×10^{-2}	1.12×10^{-1}	1.00	293	CI
LC–293–4	2.56×10^{-2}	1.16×10^{-1}	0.99	293	CL
LC–293–4	2.08×10^{-2}	1.69×10^{-1}	0.44	293	DL
LC–293–5	9.31×10^{-4}	7.37×10^{-2}	1.00	293	CI
LC–293–5	3.65×10^{-4}	7.81×10^{-2}	0.15	293	CL
LC–293–5	3.25×10^{-3}	4.36×10^{-2}	0.96	293	DL
LC–293–6	4.62×10^{-3}	1.32×10^{-1}	1.00	293	CI
LC–293–6	4.18×10^{-3}	1.34×10^{-1}	0.89	293	CL
LC–293–6	1.47×10^{-2}	3.55×10^{-2}	0.90	293	DL
LC–293–7	***1.22×10^{-1}***	***-6.02×10^{-2}***	1.00	293	CI
LC–293–7	***1.23×10^{-1}***	***-6.55×10^{-2}***	0.99	293	CL
LC–293–7	1.03×10^{-1}	9.36×10^{-2}	0.79	293	DL
LC–293–8	4.50×10^{-2}	5.44×10^{-2}	1.00	293	CI
LC–293–8	4.57×10^{-2}	5.14×10^{-2}	1.00	293	CL
LC–293–8	3.96×10^{-2}	9.84×10^{-2}	0.79	293	DL
LC–293–9	***2.86×10^{-2}***	***-8.65×10^{-3}***	0.97	293	CI
LC–293–9	2.30×10^{-2}	1.68×10^{-2}	0.80	293	CL
LC–293–9	***6.46×10^{-2}***	***-2.93×10^{-1}***	0.89	293	DL
LC–293–10	***6.20×10^{-2}***	***-2.66×10^{-2}***	0.99	293	CI
LC–293–10	***5.44×10^{-2}***	***-8.96×10^{-4}***	0.94	293	CL
LC–293–10	***9.34×10^{-2}***	***-1.91×10^{-1}***	0.54	293	DL
LC–416–1	***5.51×10^{-2}***	***-9.88×10^{-3}***	1.00	416	CI
LC–416–1	4.86×10^{-2}	1.78×10^{-2}	0.95	416	CL
LC–416–1	***6.34×10^{-2}***	***-6.52×10^{-2}***	0.89	416	DL
LC–416–2	3.87×10^{-2}	8.11×10^{-3}	1.00	416	CI
LC–416–2	***5.73×10^{-2}***	***-2.09×10^{-2}***	1.00	416	CL
LC–416–2	2.65×10^{-2}	1.15×10^{-1}	0.48	416	DL
LC–416–3	3.13×10^{-2}	5.96×10^{-2}	1.00	416	CI
LC–416–3	3.04×10^{-2}	6.25×10^{-2}	1.00	416	CL
LC–416–3	3.71×10^{-2}	3.65×10^{-2}	0.98	416	DL
LC–416–4	***3.73×10^{-2}***	***-1.53×10^{-2}***	0.99	416	CI
LC–416–4	***3.93×10^{-2}***	***-2.44×10^{-2}***	0.98	416	CL
LC–416–4	1.70×10^{-2}	1.52×10^{-1}	0.15	416	DL
LC–416–5	4.37×10^{-3}	4.67×10^{-2}	1.00	416	CI
LC–416–5	4.66×10^{-3}	4.47×10^{-2}	0.97	416	CL
LC–416–5	1.59×10^{-3}	8.34×10^{-2}	0.49	416	DL
LC–416–6	2.38×10^{-2}	3.63×10^{-3}	1.00	416	CI

Table 6. Measured values from tension infiltrometer tests on intact core samples.—Continued

[The core identification begins with the site name, then the sample number. For example, core ID 152–4 is the fourth core from site LC–152; three analysis methods used from Vandervaere and others (2000) are the Cumulative Infiltration (CI), Cumulative Linearization (CL), and Differentiated Linearization (DL) methods ; Bolded text denotes if either field-saturated hydraulic conductivity (K_{fs}) or sorptivity (S) was a negative value, which indicates that neither the Kfs nor the S values were used in further analysis; cm s^{-1}, centimeters per second; cm $s^{-0.5}$, centimeters per square root of second; (-), dimensionless; R^2, coefficient of determination; dNBR, difference in Normalized Burn Ratio]

Sample name	K_{fs} (cm s^{-1})	S (cm $s^{-0.5}$)	R^2 (-)	dNBR (-)	Method
LC–416–6	2.38×10^{-2}	3.55×10^{-3}	1.00	416	CL
LC–416–6	2.13×10^{-2}	3.36×10^{-2}	0.76	416	DL
LC–416–7	1.05×10^{-2}	6.55×10^{-2}	1.00	416	CI
LC–416–7	9.47×10^{-3}	7.06×10^{-2}	0.96	416	CL
LC–416–7	1.36×10^{-2}	4.41×10^{-2}	0.84	416	DL
LC–416–8	***1.70×10^{-2}***	***-3.77×10^{-2}***	0.99	416	CI
LC–416–8	***1.62×10^{-2}***	***-3.32×10^{-2}***	0.98	416	CL
LC–416–8	***3.46×10^{-2}***	***-2.40×10^{-1}***	0.97	416	DL
LC–416–9	1.52×10^{-2}	5.10×10^{-2}	1.00	416	CI
LC–416–9	1.27×10^{-2}	6.01×10^{-2}	0.89	416	CL
LC–416–9	1.89×10^{-2}	3.59×10^{-2}	0.97	416	DL
LC–416–10	4.62×10^{-3}	9.51×10^{-2}	1.00	416	CI
LC–416–10	4.73×10^{-3}	9.45×10^{-2}	0.99	416	CL
LC–416–10	4.47×10^{-3}	9.96×10^{-2}	0.75	416	DL
LC–533–1	***8.61×10^{-2}***	***-2.25×10^{-1}***	1.00	533	CI
LC–533–1	***8.58×10^{-2}***	***-2.24×10^{-1}***	1.00	533	CL
LC–533–1	5.94×10^{-2}	2.32×10^{-2}	0.48	533	DL
LC–533–2	1.98×10^{-3}	1.86×10^{-2}	0.99	533	CI
LC–533–2	1.58×10^{-3}	2.37×10^{-2}	0.81	533	CL
LC–533–2	***4.17×10^{-3}***	***-2.90×10^{-2}***	0.79	533	DL
LC–533–3	***3.95×10^{-2}***	***-9.65×10^{-2}***	1.00	533	CI
LC–533–3	***3.90×10^{-2}***	***-9.38×10^{-2}***	1.00	533	CL
LC–533–3	***4.56×10^{-2}***	***-1.60×10^{-1}***	0.84	533	DL
LC–533–4	***4.34×10^{-3}***	***-1.22×10^{-3}***	1.00	533	CI
LC–533–4	***4.26×10^{-3}***	***-2.70×10^{-4}***	0.99	533	CL
LC–533–4	***6.79×10^{-3}***	***-4.72×10^{-2}***	0.99	533	DL
LC–533–6	1.02×10^{-2}	9.45×10^{-2}	1.00	533	CI
LC–533–6	1.00×10^{-2}	9.54×10^{-2}	0.99	533	CL
LC–533–6	1.29×10^{-2}	6.97×10^{-2}	0.91	533	DL
LC–533–7	8.41×10^{-3}	5.82×10^{-2}	1.00	533	CI
LC–533–7	9.21×10^{-3}	5.44×10^{-2}	0.97	533	CL
LC–533–7	2.65×10^{-3}	1.08×10^{-1}	0.76	533	DL
LC–533–8	***4.82×10^{-2}***	***-1.70×10^{-1}***	1.00	533	CI
LC–533–8	***4.81×10^{-2}***	***-1.69×10^{-1}***	1.00	533	CL
LC–533–8	***5.88×10^{-2}***	***-2.63×10^{-1}***	0.84	533	DL
LC–533–9	1.70×10^{-2}	3.22×10^{-3}	1.00	533	CI
LC–533–9	1.67×10^{-2}	5.06×10^{-3}	1.00	533	CL
LC–533–9	***2.09×10^{-2}***	***-3.17×10^{-2}***	0.97	533	DL
LC–533–10	***4.32×10^{-2}***	***-9.37×10^{-2}***	0.99	533	CI
LC–533–10	***4.09×10^{-2}***	***-8.06×10^{-2}***	0.97	533	CL
LC–533–10	***8.67×10^{-2}***	***-5.54×10^{-1}***	0.79	533	DL
LC–618–1	***7.50×10^{-2}***	***-3.56×10^{-3}***	1.00	618	CI
LC–618–1	6.90×10^{-2}	3.56×10^{-2}	0.98	618	CL
LC–618–1	7.50×10^{-2}	1.45×10^{-2}	0.61	618	DL
LC–618–2	***9.58×10^{-2}***	***-2.28×10^{-2}***	1.00	618	CI
LC–618–2	9.06×10^{-2}	2.18×10^{-2}	0.99	618	CL
LC–618–2	8.97×10^{-2}	3.24×10^{-2}	0.62	618	DL
LC–618–3	5.34×10^{-2}	2.08×10^{-2}	0.99	618	CI
LC–618–3	4.71×10^{-2}	3.77×10^{-2}	0.96	618	CL
LC–618–3	***6.85×10^{-2}***	***-2.84×10^{-2}***	0.74	618	DL
LC–618–4	5.62×10^{-2}	6.95×10^{-2}	1.00	618	CI
LC–618–4	5.61×10^{-2}	6.96×10^{-2}	1.00	618	CL
LC–618–4	6.49×10^{-2}	4.70×10^{-2}	0.81	618	DL
LC–618–5	1.77×10^{-3}	8.73×10^{-2}	1.00	618	CI
LC–618–5	1.67×10^{-3}	8.80×10^{-2}	0.86	618	CL
LC–618–5	3.29×10^{-3}	7.32×10^{-2}	0.68	618	DL
LC–618–6	***7.77×10^{-2}***	***-8.55×10^{-3}***	1.00	618	CI
LC–618–6	7.14×10^{-2}	1.52×10^{-2}	0.98	618	CL
LC–618–6	***8.93×10^{-2}***	***-4.81×10^{-2}***	0.98	618	DL
LC–618–7	***-3.50×10^{-4}***	***6.07×10^{-2}***	0.96	618	CI
LC–618–7	***-1.63×10^{-3}***	***7.76×10^{-2}***	0.50	618	CL
LC–618–7	1.97×10^{-3}	1.00×10^{-2}	0.98	618	DL
LC–618–8	***6.64×10^{-2}***	***-1.70×10^{-2}***	1.00	618	CI
LC–618–8	***6.44×10^{-2}***	***-1.05×10^{-2}***	1.00	618	CL
LC–618–8	6.04×10^{-2}	1.48×10^{-2}	0.60	618	DL
LC–618–9	4.24×10^{-2}	1.66×10^{-2}	1.00	618	CI
LC–618–9	4.31×10^{-2}	1.39×10^{-2}	1.00	618	CL
LC–618–9	2.72×10^{-2}	1.25×10^{-1}	0.67	618	DL
LC–618–10	***1.11×10^{-1}***	***-1.14×10^{-1}***	1.00	618	CI
LC–618–10	***1.08×10^{-1}***	***-1.04×10^{-1}***	0.99	618	CL
LC–618–10	***1.25×10^{-1}***	***-1.86×10^{-1}***	0.78	618	DL
LC–802–1	***5.01×10^{-2}***	***-3.97×10^{-2}***	1.00	802	CI
LC–802–1	4.98×10^{-2}	3.79×10^{-2}	1.00	802	CL
LC–802–1	4.50×10^{-2}	3.26×10^{-2}	0.78	802	DL
LC–802–2	1.10×10^{-2}	2.01×10^{-2}	0.99	802	CI
LC–802–2	1.23×10^{-2}	1.13×10^{-2}	0.96	802	CL

Table 6. Measured values from tension infiltrometer tests on intact core samples.—Continued

[The core identification begins with the site name, then the sample number. For example, core ID 152–4 is the fourth core from site LC–152; three analysis methods used from Vandervaere and others (2000) are the Cumulative Infiltration (CI), Cumulative Linearization (CL), and Differentiated Linearization (DL) methods ; Bolded text denotes if either field-saturated hydraulic conductivity (K_{fs}) or sorptivity (S) was a negative value, which indicates that neither the Kfs nor the S values were used in further analysis; cm s^{-1}, centimeters per second; cm $s^{-0.5}$, centimeters per square root of second; (-), dimensionless; R^2, coefficient of determination; dNBR, difference in Normalized Burn Ratio]

Sample name	K_{fs} (cm s^{-1})	S (cm $s^{-0.5}$)	R^2 (-)	dNBR (-)	Method
LC–802–2	1.04×10^{-3}	1.47×10^{-1}	0.37	802	DL
LC–802–3	***3.83×10^{-2}***	***-4.05×10^{-2}***	0.98	802	CI
LC–802–3	2.97×10^{-2}	3.63×10^{-3}	0.86	802	CL
LC–802–3	***6.26×10^{-2}***	***-2.41×10^{-1}***	0.83	802	DL
LC–802–4	***1.21×10^{-2}***	***-3.16×10^{-2}***	0.99	802	CI
LC–802–4	***1.12×10^{-2}***	***-2.46×10^{-2}***	0.95	802	CL
LC–802–4	***1.96×10^{-2}***	***-1.32×10^{-1}***	0.57	802	DL
LC–802–5	8.85×10^{-3}	5.54×10^{-2}	0.99	802	CI
LC–802–5	1.07×10^{-2}	4.39×10^{-2}	0.91	802	CL
LC–802–5	2.72×10^{-3}	1.35×10^{-1}	0.07	802	DL
LC–802–6	1.27×10^{-3}	4.87×10^{-2}	1.00	802	CI
LC–802–6	1.13×10^{-3}	5.02×10^{-2}	0.92	802	CL
LC–802–6	2.97×10^{-3}	1.48×10^{-2}	0.98	802	DL
LC–802–7	2.60×10^{-2}	4.51×10^{-2}	1.00	802	CI
LC–802–7	2.54×10^{-2}	4.74×10^{-2}	1.00	802	CL
LC–802–7	2.82×10^{-2}	3.43×10^{-2}	0.65	802	DL
LC–802–8	***1.55×10^{-2}***	***-4.41×10^{-3}***	1.00	802	CI
LC–802–8	***1.55×10^{-2}***	***-4.55×10^{-3}***	1.00	802	CL
LC–802–8	1.15×10^{-2}	4.17×10^{-2}	0.60	802	DL
LC–802–9	3.40×10^{-4}	9.56×10^{-2}	1.00	802	CI
LC–802–9	2.31×10^{-4}	9.64×10^{-2}	0.28	802	CL
LC–802–9	6.99×10^{-4}	9.11×10^{-2}	0.19	802	DL
LC–802–10	2.48×10^{-3}	5.91×10^{-2}	1.00	802	CI
LC–802–10	2.24×10^{-3}	6.12×10^{-2}	0.97	802	CL
LC–802–10	3.74×10^{-3}	4.18×10^{-2}	0.96	802	DL
LC–922–1	4.92×10^{-2}	4.36×10^{-3}	1.00	922	CI
LC–922–1	4.95×10^{-2}	3.48×10^{-3}	1.00	922	CL
LC–922–1	4.61×10^{-2}	4.72×10^{-2}	0.60	922	DL
LC–922–2	1.24×10^{-2}	5.35×10^{-2}	0.97	922	CI
LC–922–2	5.29×10^{-3}	7.83×10^{-2}	0.28	922	CL
LC–922–2	***3.26×10^{-2}***	***-4.79×10^{-2}***	0.94	922	DL
LC–922–3	3.00×10^{-2}	4.74×10^{-2}	0.98	922	CI
LC–922–3	2.21×10^{-2}	6.79×10^{-2}	0.78	922	CL
LC–922–3	***7.30×10^{-2}***	***-1.20×10^{-1}***	0.95	922	DL
LC–922–4	***-1.87×10^{-4}***	***9.69×10^{-2}***	0.99	922	CI
LC–922–4	***-6.63×10^{-4}***	***1.00×10^{-1}***	0.19	922	CL
LC–922–4	***8.22×10^{-3}***	***-1.01×10^{-2}***	0.98	922	DL
LC–922–5	9.60×10^{-3}	4.60×10^{-2}	1.00	922	CI
LC–922–5	8.34×10^{-3}	5.10×10^{-2}	0.92	922	CL
LC–922–5	1.51×10^{-2}	1.61×10^{-2}	0.95	922	DL
LC–922–6	3.33×10^{-2}	1.31×10^{-1}	1.00	922	CI
LC–922–6	2.82×10^{-2}	1.53×10^{-1}	0.94	922	CL
LC–922–6	3.99×10^{-2}	1.07×10^{-1}	0.47	922	DL
LC–922–7	***2.97×10^{-2}***	***-8.24×10^{-3}***	1.00	922	CI
LC–922–7	***2.83×10^{-2}***	***-1.82×10^{-3}***	0.98	922	CL
LC–922–7	***4.76×10^{-2}***	***-1.52×10^{-1}***	0.97	922	DL
LC–922–8	3.09×10^{-2}	3.42×10^{-2}	1.00	922	CI
LC–922–8	3.11×10^{-2}	3.33×10^{-2}	1.00	922	CL
LC–922–8	2.44×10^{-2}	8.95×10^{-2}	0.56	922	DL
LC–922–9	2.97×10^{-2}	3.94×10^{-2}	1.00	922	CI
LC–922–9	2.90×10^{-2}	4.28×10^{-2}	1.00	922	CL
LC–922–9	3.41×10^{-2}	1.32×10^{-2}	0.97	922	DL
LC–922–10	3.96×10^{-2}	6.29×10^{-3}	1.00	922	CI
LC–922–10	4.10×10^{-2}	1.04×10^{-3}	0.99	922	CL
LC–922–10	1.36×10^{-2}	2.01×10^{-1}	0.32	922	DL

Sorptivity (S)

Sorptivity was also not inversely correlated with burn severity. Sorptivity ranged from approximately 10^{-1} to 10^{-2} centimeter per square root of second (cm $s^{-0.5}$) for the full range of dNBR sampled (tables 6 and 7, fig. 16) and showed no dependence on dNBR, MTBS thematic burn-severity class, or BARC4 thematic class. Similarly to K_{fs}, the number of viable infiltrometer results (K_{fs} and S are > 0) did not depend on the method of infiltrometer data analysis (that is, CI, CL, or DL method) (tables 6 and 7). A linear regression through the geometric means of the DL method S values also suggests a slightly increasing trend for S with increasing dNBR, which was again contrary to expectations (fig. 16). The small R^2 value of 0.25 for the linear regression and large spread in values, based on ± one standard deviation, suggests there is no strong relation between S and dNBR at this site 4 years after the wildfire (fig. 16*B*). Like the K_{fs} analysis, this was the same technique used by Moody and others (2016) to identify relations between S and dNBR at the Black Forest Fire site in Colorado. The F-test p-value for the geometric mean of S regressed against dNBR is 0.161, which exceeds the threshold p-value of 0.05; therefore, the trends in the regressions are not indicated to be significant within the assumptions of the statistical test.

Table 7. Geometric mean values of soil-hydraulic properties of field-saturated hydraulic conductivity (K_{fs}) and sorptivity from replicate tension infiltration measurements on intact soil cores.

[CI, three analysis methods used are the Cumulative Infiltration; CL, Cumulative Linearization; DL, Differentiated Linearization methods from Vandervaere and others (2000); n, number of measurements used in the geometric mean, which is less than the number of samples analyzed because if either K_{fs} or sorptivity (S) was a negative value, then neither of those values was used in the geometric mean calculation; σ, standard deviation of the DL values; dNBR, difference in normalized burn ratio; cm s^{-1}, centimeters per second; cm $s^{-0.5}$, centimeters per square root of seconds]

Site name		K_{fs}							S						
		CI		CL		DL	σ		CI		CL		DL	σ	
	dNBR	(cm s^{-1})	n	(cm s^{-1})	n	(cm s^{-1})	(cm s^{-1})	n	(cm $s^{-0.5}$)	n	(cm $s^{-0.5}$)	n	(cm $s^{-0.5}$)	(cm $s^{-0.5}$)	n
LC–152	152	4.91×10^{-3}	6	5.85×10^{-3}	7	4.57×10^{-3}	1.70×10^{-2}	9	3.52×10^{-2}	6	3.76×10^{-2}	7	8.22×10^{-3}	2.74×10^{-2}	9
LC–293	293	7.12×10^{-3}	5	8.20×10^{-3}	7	1.28×10^{-2}	3.62×10^{-2}	7	6.03×10^{-2}	5	3.78×10^{-2}	7	4.43×10^{-2}	5.73×10^{-2}	7
LC–416	416	1.37×10^{-2}	7	1.37×10^{-2}	7	1.26×10^{-2}	1.15×10^{-2}	8	3.08×10^{-2}	7	3.55×10^{-2}	7	6.40×10^{-2}	4.45×10^{-2}	8
LC–533	533	7.33×10^{-3}	4	7.02×10^{-3}	4	1.27×10^{-2}	3.02×10^{-2}	3	2.40×10^{-2}	4	2.81×10^{-2}	4	5.59×10^{-2}	4.25×10^{-2}	3
LC–618	618	2.18×10^{-2}	4	3.64×10^{-2}	7	2.40×10^{-2}	3.52×10^{-2}	7	3.81×10^{-2}	4	3.24×10^{-2}	7	3.14×10^{-2}	4.17×10^{-2}	7
LC–802	802	3.73×10^{-3}	6	6.42×10^{-3}	8	4.88×10^{-3}	1.62×10^{-2}	8	4.90×10^{-2}	6	3.15×10^{-2}	8	5.18×10^{-2}	5.05×10^{-2}	8
LC–922	922	2.61×10^{-2}	8	2.18×10^{-2}	8	2.61×10^{-2}	1.33×10^{-2}	6	2.95×10^{-2}	8	2.61×10^{-2}	8	5.18×10^{-2}	7.08×10^{-2}	6

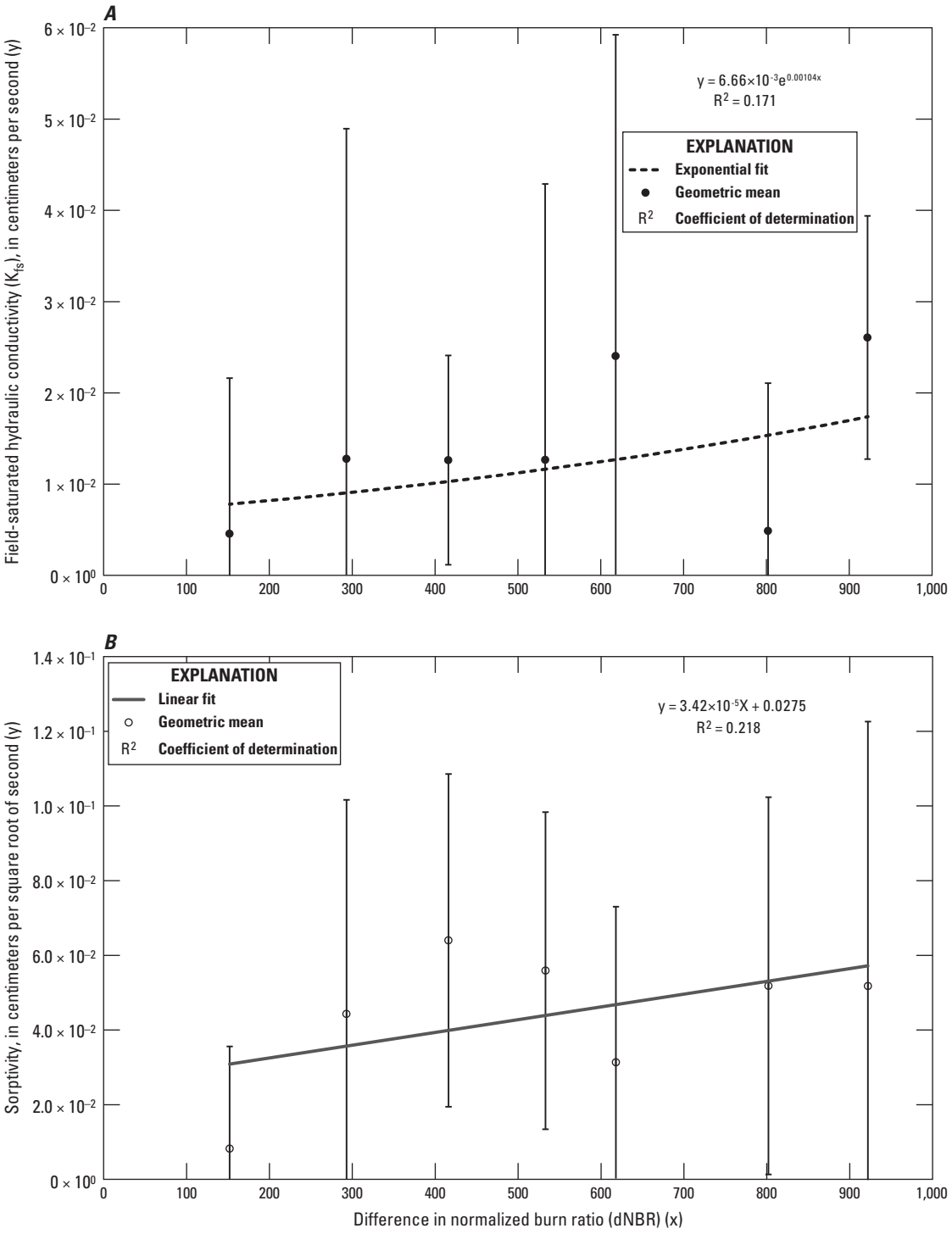

Figure 16. *A*, the geometric mean of field-saturated hydraulic conductivity (K_{fs}) as a function of difference in Normalized Burn Ratio (dNBR) with a least-squares exponential regression; and *B*, the geometric mean of sorptivity as a function of dNBR with a least-squares linear regression. Geometric mean values are calculated on the differentiated linearization (DL) method data and the error bars are ± one standard deviation.

Comparisons to Previous Studies and Implications

The results of this work were surprising in that SPPs showed clear differences depending on dNBR and the SHPs did not. These results also indicate that SPP differences as a function of burn severity cannot be used as reliable indicators of SHP differences as a function of burn severity.

The reductions in LOI with increasing dNBR for the 0–1 cm depth concur with prior work by Alauzis and others (2004) and Hatten and Zabowski (2009), who showed that changes in soil organic matter after fire depended on burn severity. The mean LOI values of 30.5 and 43.3 percent (table 4) at the lower severity sites (LC–152 and LC–293, respectively) are larger but similar in magnitude to unburned LOI values of 11.2 to 20.0 percent reported by Ebel (2012). The mean LOI values of 6.0 and 8.4 percent (table 4) at the highest severity sites (LC–802 and LC–922, respectively) are similar to high-severity burn LOI values of 3.1 to 5.8 percent reported by Ebel (2012) and Moody and others (2005). The comparative data from these previous studies were collected from wildfires in the Colorado Front Range. The bulk density results for the 0–1cm depth showed an increase in bulk density with increasing burn severity (table 4, fig. 11), which agrees with work by Certini (2005). The magnitude of the increase in bulk density is similar to prior results for near-surface soil affected by fire shown in studies by Giovannini and others (1988), Andreu and others (2001), Stoof and others (2010), and Jordán and others (2011). The soil-particle size distributions from this study area showed increases in gravel, declines in organic fraction, and decreases in fines with increasing dNBR. Previous research on wildfire effects on soil-particle size distribution has shown aggregation of fines (clay and silt) that can increase the sand fraction of the particle-size distribution at the expense of fines (Ulery and Graham, 1993; Molina and Sanroque, 1996; Giovannini and Lucchesi, 1997). Although the soil-particle sizes reported in this study show a decline in fines for higher severity sites, no increase in the sand fraction was observed. This suggests that the changes in soil-particle size distribution may be the result of a process other than the aggregation of fines.

The K_{fs} magnitudes reported in this study are one to two orders of magnitude greater than the geometric mean burned K_{fs} value from Ebel and Moody (2017) of 1.4×10^{-3} cm/ s^{-1}, which is based on nine values from around the world. The S values reported in this study are approximately 1 to 6 times greater than the geometric mean burned S value from Ebel and Moody (2017) of 9.9×10^{-3} cm/s^{-1}.

It is important to note that the timing of postwildfire measurements reported in this study (4 years after the wildfire) is atypical of the timing of most postwildfire measurements which usually occur within days to months of wildfire containment. In particular, and although speculative, it is possible there were substantial reductions in infiltration rates corresponding to the reductions in SHPs immediately following the wildfire, but that SHPs that control infiltration have returned to magnitudes that do not facilitate appreciable runoff generation during rainfall at these sites. The SPPs of bulk density and soil organic matter (from loss on ignition measurements) reflect the fire effects on near-surface soil. The SPP of particle size, however, may reflect the development of a coarse lag deposit and winnowing, or preferential removal of fines that result from repeated overland flow and erosion events. Development of surficial lag deposits in response to repeated overland flow events following rainfall after wildfire has been observed at other locations in the western United States (Morris and Moses, 1987; Pierson and others, 2002; Wohl, 2013; Hyde and others, 2015; Rengers and others 2016). It is established that the East Fork Jemez River, Peralta Canyon, and other areas in the watersheds below the sampling sites experienced flooding (National Geographic, 2011; Reale and others, 2015); however, it is not established how the surface conditions of infiltration and particle-size distributions evolved in the 4 years after the 2011 wildfire. Future research should address the coevolution and feedbacks between SHPs that control infiltration and physical properties including particle-size distributions.

Limitations

The work presented in this study has some limitations that prevent more certain determination of why the SPPs differed across burn severity whereas the SHPs did not. In order to determine the temporal evolution of SPPs and SHPs, several measurement campaigns would be needed from immediately after the burn until no further change is detected. In this study, only one measurement campaign was conducted in the 4 years following the 2011 wildfire. These future campaigns could focus on SPPs and SHPs over time as a function of burn severity at the same field location and to link recovery to a more detailed, process-based framework. The remotely sensed burn-severity metric dNBR could also be improved, given that the metric mixes vegetation and soil burn-severity effects. Hyperspectral imagery after wildfire may be capable of more direct identification of soil burn-severity classes (Lewis and others, 2008, 2011) that can be linked to SHP changes as a function of burn severity.

Summary

The generation of runoff and the resultant flash flooding can be substantially larger following wildfire than for similar prewildfire rainstorms. Flash flooding for several years after the 2011 Las Conchas Fire in New Mexico provided the motivation for this investigation of soil-physical properties (SPPs) and soil-hydraulic properties (SHPs) that affect infiltration and the subsequent runoff generation. The dNBR (difference in Normalized Burn Ratio) metric guided sample collection across a full spectrum of burn severities that cover the range of Monitoring Trends in Burn Severity program (MTBS) and Burned Area Reflectance Classification (BARC4) thematic classes from low to high severity. Fourteen random soil cores were collected at each of the sampling sites for laboratory analysis. Physical properties of initial and saturated soil-water content, bulk density, soil organic matter, and soil-particle size along with soil hydraulic properties of field saturated hydraulic conductivity (K_{fs}) and sorptivity (S) were measured.

The SHPs were estimated using tension infiltrometer measurements and three different data analysis methods: (1) cumulative infiltration (CI), (2) differentiated linearization (DL), and (3) cumulative linearization (CL). The CI method determines the values of saturated hydraulic conductivity (Ks) and S using measured soil infiltration data and the Phillips (1969) infiltration equation that gives infiltration as a function of time. However, the CI method requires ideal soil conditions that are not often present in fire-affected soils. The DL and CL methods use linearization of the same infiltration equation to identify infiltration conditions where the CI method is not valid; these conditions include infiltration across different infiltration regimes and infiltration that is controlled by the overlying contact sand (if used) instead of the actual soil core.

Infiltration data from each of the samples were plotted with the CI, DL, and CL methods. Valid data subsets for using these methods were identified with the DL and CL methods. Each of the three methods was then applied to the new data subsets to estimate *Ks* and *S* values.

The SPPs and SHPs had different dependence on the remotely sensed burn-severity metric dNBR for seven sites. The SPP measurements showed large effects of burn severity, focused in the top 1 centimeter (cm) of soil, on bulk density and soil organic matter. The threshold of these effects was between 300 and 400 dNBR, which corresponds to a MTBS thematic class between moderate and high burn severity and a BARC4 thematic class of high severity. Gravel content and the content of fines in the top 1 cm of soil had a higher threshold value between 450 and 500 dNBR. Lesser effects on SPPs were observed at depths of 1–3 cm and 3–6 cm, reflecting a decrease in the influence from wildfire with depth.

In contrast, SHPs did not show appreciable relationships to dNBR or MTBS/BARC4 thematic classes. It is conceivable that less than 4 years may be the time required for SHP recovery following wildfire in this area. These results also indicate that SPP differences as a function of burn severity cannot be used as reliable indicators of SHP differences as a function of burn severity.

Future research should address the coevolution and feedback between SHPs that control infiltration and physical properties. This could be accomplished by collecting soil samples for a period from immediately after to many years following a wildfire.

References Cited

Alauzis, M.V., Mazzarino, Maria, Raffaele, Estela, and Roselli, Lucía, 2004, Wildfires in NW Patagonia: Long-term effects on a Nothofagus forest soil: Forest Ecology and Management. v. 192, p. 131-142. https://doi.org/10.1016/j.foreco.2003.11.014.

Andreu, V., Imeson, A.C., and Rubio, J.L., 2001, Temporal changes in soil aggregates and water erosion after a wildfire in a Mediterranean pine forest: Catena, v. 44, no. 1, p. 69–84.

Balch, J.K., Bradley, B.A., Abatzogloue, J.T., Nagy, R.C., Fuscod, E.J., and Mahood, A.L., 2017, Human-started wildfires expand the fire niche across the United States: Proceedings of the National Academy of Sciences of the United States of America, accessed June 2017 at http://www.pnas.org/content/114/11/2946.full.pdf.

Certini, Giacomo, 2005, Effects of fire on properties of forest soils—A review: Oecologia, v. 143, p. 1–10. https://doi.org/10.1007/s00442-004-1788-8.

Cocke, A.E., Fule, P.Z., and Crouse, J.E., 2005, Comparison of burn severity assessments using Differenced Normalized Burn Ratio and ground data: International Journal of Wildland Fire, v. 14, p. 189–198.

Cook, F.J., 2007, Unsaturated hydraulic conductivity—Laboratory tension infiltrometer *in* Carter, M.R., and Gregorich, E.G., eds., Soil sampling and methods of analysis: Boca Raton, Florida, CRC Press, p. 1075–1087.

Decagon Devices, 2013, Mini disk infiltrometer user's manual version 10: Pullman, Washington, Decagon Devices, Inc., 30 p.

Doerr, S.H., Shakesby, R.A., and Walsh, R.P.D., 2000, Soil water repellency—Its causes, characteristics and hydro-geomorphological significance: Earth-Science Reviews, v. 15, p. 33–65.

Ebel, B.A., 2012. Wildfire impacts on soil-water retention in the Colorado Front Range, United States: Water Resources Research, v. 48, no. 12, p. W12515.

Ebel, B.A., and Moody, J.A., 2017, Synthesis of soil-hydraulic properties and infiltration timescales in wildfire-affected soils: Hydrological Processes, v. 31, no. 2, p. 324–340.

Ebel, B.A., Moody, J.A., and Martin, D.A., 2012, Hydrologic conditions controlling runoff generation immediately after wildfire: Water Resources Research, v. 48, p. W03529, https://doi.org/10.1029/2011WR011470.

Ebel, B.A., and Romero, Orlando, 2017, Soil physical and hydraulic properties in the area affected by the 2011 Las Conchas fire in New Mexico (ver.1.1, August 2017): U.S. Geological Survey data release at https://doi.org/10.5066/F71834RB.

Fisher, R.A.,1922, On the interpretation of $\chi 2$ from contingency tables, and the calculation of P: Journal of the Royal Statistical Society, v. 85, no. 1, p. 87–94, http://dx.doi.org/10.2307/2340521.

Garrity, S.R., Allen, C.D., Brumby, S.P., Gangodagamage, C., McDowell, N.D., and Cai, D.M., 2013, Quantifying tree mortality in a mixed species woodland using multitemporal high spaial resolution satellite imagery: Remote Sensing of Environment, v. 129, p. 54–65.

Giovannini, G., and Lucchesi, S., 1997, Modifications induced in soil physico-chemical parameters by experimental fires at different intensities: Soil Science, v. 162, p. 479–486.

Giovannini, G., Lucchesi, S., and Giachetti, M., 1988, Effects of heating on some physical and chemical parameters related to soil aggregation and erodibility: Soil Science, v. 146, p. 255–261.

Guy, H.P., 1969, Laboratory theory and methods for sediment analysis: U.S. Geological Survey Techniques of Water-Resources Investigations, book 5, chap. C1, 58 p. [Also available at https://pubs.er.usgs.gov/publication/twri05C1.]

Hatten, Jeff and Zabowski, D, 2009, Changes in Soil Organic Matter Pools and Carbon Mineralization as Influenced by Fire Severity: Soil Science Society of America Journal, v. 73, no. 1, p. 262-273, https://doi.org/10.2136/sssaj2007.0304.

Haverkamp, R., Ross, P.J., Smettem, K.R.J., and Parlange, J.Y., 1994, Three-dimensional analysis of infiltration from the disc infiltrometer. 2. Physically based infiltration equation: Water Resources Research, v. 30, issue 11, p. 2931–2935, https://doi.org/10.1029/94WR01788.

Heiri, O., Lotter, A. F., and Lemcke, G., 2001, Loss on ignition as a method for estimating organic and carbonate content in sediments—Reproducibility and comparability of results: Journal of Paleolimnology, v. 25, p. 101–110, https://doi.org/10.1023/A:1008119611481.

Hyde, K.D., Jencso, K., Wilcox, A.C., and Woods, S., 2015, Influences of vegetation disturbance on hydrogeomorphic response following wildfire: Hydrological Processes, v. 30, p. 1131–1148, https://doi.org/10.1002/hyp.10691.

Jordán, A., Zavala, L.M., Mataix-Solera, J., Nava, A.L., and Alanís, N., 2011, Effect of fire severity on water repellency and aggregate stability on Mexican volcanic soils: Catena, v. 84, no. 3, p.136–147.

Keely, J.E., 2009, Fire intensity, fire severity and burn severity—A brief review and suggested usage: International Journal of Wildland Fire, v. 18, p. 116–126.

Key C.H., and Benson N.C., 2006, Landscape assessment—Remote sensing of severity, the Normalized Burn Ratio; and ground measure of severity, the Composite Burn Index, *in* FIREMON: Fire Effects Monitoring and Inventory System: U.S. Department of Agriculture, Forest Service, Rocky Mountain Research Station, General Technical Report RMRS–GTR–164–CD; LA-1–55.

Letey, J., 2001, Causes and consequences of fire-induced soil water repellency: Hydrological Processes, v. 15, p. 2867–2875.

Lewis, S.A., Robichaud, P.R., Frazier, B.E., Wu, J.Q., and Laes, D.Y., 2008, Using hyperspectral imagery to predict post-wildfire soil water repellency: Geomorphology, v. 95, no. 3, p.192–205.

Lewis, S.A., Hudak, A.T., Ottmar, R.D., Robichaud, P.R., Lentile, L.B., Hood, S.M., Cronan, J.B., and Morgan, P., 2011, Using hyperspectral imagery to estimate forest floor consumption from wildfire in boreal forests of Alaska, USA: International Journal of Wildland Fire, v. 20, p. 255–271.

Miller, J.D., and Thode, A. E., 2007, Quantifying burn severity in a heterogeneous landscape with a relative version of the delta Normalized Burn Ratio (dNBR): Remote Sensing of Environment, v. 109, p. 66-80.

Molina, M.J., and Sanroque, P., 1996, Impact of forest fires on desertification processes—A review in relation to soil erodibility, *in* Soil Degradation and Desertification in Mediterranean Environments, Rubio, J.L., and Calvo, A., eds.: Logrono, Spain, Geoforma Ediciones, p. 145–163.

Monitoring Trends in Burn Severity (MTBS), 2017, accessed November 27, 2017, at https://www.mtbs.gov/.

Moody, J. A., Smith, J. D., and Ragan, B. W., 2005, Critical shear stress for erosion of cohesive soils subjected to temperatures typical of wildfires: Journal of Geophysical Research: Earth Surface, v. 110(F1), https://doi.org/10.1029/2004JF000141.

Moody, J.A., Ebel, B.A., Nyman, P., Martin, D.A., Stoof, C.R., and Randy McKinley, 2016, Relations between soil hydraulic properties and burn severity: International Journal of Wildland Fire, v. 25, p. 279–293.

Morris, S. E. and Moses, T. A., 1987, Forest fire and the natural soil erosion regime in the Colorado Front Range: Annals of the Association of American Geographers, v. 77, no. 2, p. 245–254.

National Aeronautics and Space Administration, 2017, Landsat Science – The thematic mapper, accessed April 2017 at https://landsat.gsfc.nasa.gov/the-thematic-mapper.

National Aeronautics and Space Administration, 2017, Landsat Science —Landsat then and now, accessed September 2017 at https://landsat.gsfc.nasa.gov/about/.

National Geographic, 2011, Fire and rain—The one-two punch of flooding after blazes: National Geographic Voices, accessed on March 24, 2017, at http://voices.nationalgeographic.com/2011/08/31/fire-and-rain/.

National Wildfire Coordinating Group, 2006, Glossary of wildland fire terminology. NWCG Incident Operations Standards Working Team., accessed November 27, 2017 at https://www.nwcg.gov/glossary/a-z.

National Wildlife Federation, 2008, Increased risk of catastrophic wildfires—Global warming's wake-up call for the Western United States, accessed November 27, 2017, at http://www.nwf.org/~/media/PDFs/Global-Warming/NWF_WildFiresFinal.ashx.

Parsons, A., Robichaud, P.R., Lewis, S.A., Napper, C., and Clark, J.T., 2010, Field guide for mapping post-fire soil burn severity: U.S. Department of Agriculture, Forest Service, General Technical Report RMRS–GTR–243, Fort Collins, Colo., Rocky Mountain Research Station, 49 p.

Patterson, M.W., 1997, Forest fires and drought in the U.S. Southwest: the University of Arizona Department of Geography and Regional Development, University of Arizona *in* Proceedings Impact of Climate Change and Land Use in the Southwestern United States interactive workshop, accessed December 2016 at https://geochange.er.usgs.gov/sw/impacts/biology/fires_drought.

Philip, J.R., 1969, Theory of infiltration—Advances in Hydroscience, v. 5, p. 215–296.

Pierson, F.B., Carlson, D.H., and Spaeth, K.E., 2002, Impacts of wildfire on soil hydrological properties of steep sagebrush-steppe rangeland: International Journal of Wildland Fire, v. 11, p. 145–151.

Reale, J.K., Van Horn, D.J., Condon, K.E. and Dahm, C.N., 2015, The effects of catastrophic wildfire on water quality along a river continuum: Freshwater Science, v. 34, p. 1426–1442.

Rengers, F.K., Tucker, G.E., Moody, J.A., and Ebel, B.A., 2016, Illuminating wildfire erosion and deposition patterns with repeat terrestrial lidar: Journal of Geophysical Research: Earth Surface, v. 121, p. 588–608, https://doi.org/10.1002/2015JF003600.

Schoeffler, F.J., and Wachter, J.B., 2015, Dynamic fire weather associated with the June 2011 New Mexico (USA) Las Conchas Fire: Phoenix, Arizona, American Meteorological Society Annual Meeting, 95th, January 4–8, 2015.

Stoof, C.R., Wesseling, J.G., and Ritsema, C.J., 2010, Effects of fire and ash on soil water retention: Geoderma, v. 159, p. 276–285, https://doi.org/10.1016/j.geoderma.2010.08.002.

Tillery, A.C., Darr, M.J., Cannon, S.C., and Michael, J.A., 2011, Postwildfire preliminary debris flow hazard assessment for the area burned by the 2011 Las Conchas Fire in north-central New Mexico: U.S. Geological Survey Open-File Report 2011–1308, accessed May 2016 at http://pubs.usgs.gov/of/2011/1308/.

Topp, G.C., and Ferre, P.A., 2002, Methods for measurement of soil water content— Thermogravimetric using convective oven-drying, *in* Dane, J.H., and Topp, G.C., eds., Methods of Soil Analysis. Part 4: Physical Methods: Soil Science Society of America Book Series 5: Madison, Wisconsin, Soil Science Society of America, p. 422–424.

Trader, L.L., 2012, Biotic and abiotic factors contributing to New Mexico's largest wildfire— The Las Conchas fire: National Park Service, Fire Ecology Program, Rx Effects, v. 1, no. 11, accessed May 2016 at https://www.nps.gov/fire/wildland-fire/resources/documents/rx-effects-spring-2012.pdf.

Ulery, A.L., and Graham, R.C., 1993, Forest fire effects on soil color and texture: Soil Science Society of America Journal, v. 57, p. 135–140.

University of California Davis [2016], UC Davis Soil Resource Laboratory web page, accessed March 2016 at https://casoilresource.lawr.ucdavis.edu/gmap/.

U.S. Department of Agriculture, Forest Service (USDA–FS), 2011, Burned-area report: USDA-Forest Service Report FS–2500–8, accessed May 2016 at http://inciweb.nwcg.gov/incident/article/2406/12416/.

U.S. Department of Agriculture, Natural Resources Conservation Service (USDA, NRCS), 2008, Soil quality indicators—Bulk Density: Soil Quality Physical Indicator Information Sheet Series, accessed May 2017 at https://www.nrcs.usda.gov/Internet/FSE_DOCUMENTS/nrcs142p2_053256.pdf.

U.S. Department of Agriculture, Natural Resources Conservation Service, 2016, Web soil survey, accessed March 2016 at http://websoilsurvey.nrcs.usda.gov/app/HomePage.htm.

U.S. Environmental Protection Agency, 2016, Climate change indicators—Wildfires, accessed December 2016 at https://www.epa.gov/climate-indicators/climate-change-indicators-wildfires.

U.S. Forest Service, 2017, Burned area emergency response (BAER) imagery support: U.S. Forest Service Remote Sensing Application Center, accessed November 27, 2017, at https://www.fs.fed.us/eng/rsac/baer/.

Vandervaere J.P., Vauclin, M., and Elrick, D.E., 2000, Transient flow from tension Infiltrometers: I. The two-parameter equation: Soil Science Society of America Journal, v. 64, p. 1263–1272.

Wohl, E., 2013, Migration of channel heads following wildfire in the Colorado Front Range, USA: Earth Surface Processes and Landforms, v. 38, p. 1049–1053.

Zhang, R. 1997, Determination of soil sorptivity and hydraulic conductivity from the disk infiltrometer: Soil Science Society of America Journal, v. 61, p. 1024–1030.

For more information about this publication, contact
Director
USGS, New Mexico Water Science Center
6700 Edith Blvd NE
Albuquerque, NM 87113

For additional information visit https://www.usgs.gov/centers/nm-water

Publishing support provided by the
Lafayette Publishing Service Center

ISSN 2328-0328 (online)
https://doi.org/10.3133/sir20185028